3D PRINTABLE AND COMPUTATIONAL MODELS OF THE BONE MARROW

MECHANICAL ENVIRONMENT

by

Alexander Regner

A thesis

submitted in partial fulfillment

of the requirements for the degree of

Master of Science in Materials Science and Engineering

Boise State University

May 2021

BOISE STATE UNIVERSITY GRADUATE COLLEGE

DEFENSE COMMITTEE AND FINAL READING APPROVALS

of the thesis submitted by

Alexander Regner

Thesis Title: 3D Printable Models of Bone Marrow Mechanical Environment

Date of Final Oral Examination: 14 April 2021

The following individuals read and discussed the thesis submitted by student Alexander Regner, and they evaluated the student's presentation and response to questions during the final oral examination. They found that the student passed the final oral examination.

Gunes Uzer, Ph.D.	Chair, Supervisory Committee
Danielle Wu, Ph.D.	Member, Supervisory Committee
Clare Fitzpatrick, Ph.D.	Member, Supervisory Committee
Trevor Lujan, Ph.D.	Member, Supervisory Committee
David Estrada, Ph.D.	Member, Supervisory Committee

The final reading approval of the thesis was granted by Gunes Uzer, Ph.D., Chair of the Supervisory Committee. The thesis was approved by the Graduate College.

DEDICATION

Thank you to my parents for everything they've done and the support they have shown me through the pursuit of my degrees. Thank you to Starr Johnson and Karen Dreher for their support in both my undergraduate and graduate degrees. Thank you to my partner, Kali Woods, for supporting me in my final push to finish.

ACKNOWLEDGMENTS

ABSTRACT

Aged individuals and astronauts experience bone loss despite rigorous physical activity. Bone mechanoresponse is in part regulated by mesenchymal stem cells (MSCs). We reported that daily low intensity vibration (LIV) restores MSC proliferation in senescence and simulated microgravity models, suggesting reduced mechanical signal delivery to MSCs likely contributes to declining bone mechanoresponse. To this end, we have developed a 3D bone marrow analog which controls trabecular geometry, marrow mechanics and external stimuli.

Finite element (FE) models of hydrogels, representing bone marrow, were generated using instantaneous compression (1000% strain/s, 20% strain) and relaxation experiments (100s) of both gelatin and hyaluronin-based hydrogels. Experimental and in silico vibration experiments using molded-gelatin wells (widths= 4 , 5, 6 and 8 mm) were performed under 1g acceleration, 100 Hz for FE model calibration.

For MSC experiments, 0.25cmgyroid-based trabeculae of bone volume fractions (BV/TV) corresponding to adult (25%) and aged (13%) mice were printed using polylactic acid. MSCs encapsulated (1×10^6 cells/mL) in migration-permissive hydrogelswithin printed trabeculae were exposed to LIV (1g, 100 Hz, 1 hour/day). After 14 days, type-I collagen, Ki-67, f-actin (n=3/grp) were quantified for extracellular matrix composition, proliferation, and morphology and grouped with respect to the maximum von Mises strain for 13.5% and 25% BV/TV scaffolds using the calibrated FE models.

TABLE OF CONTENTS

LIST OF TABLES

LIST OF FIGURES

LIST OF PICTURES

LIST OF ABBREVIATIONS

MSC	Mesenchymal Stem Cells
LIV	Low Intensity Vibration
HA	Hyaluronic Acid
PLA	Poly-lactic Acid
DIC	Digital Image Correlation
FE	Finite Element
YAP	Yes-associated Protein
CCNA	Cyclin-A2
CCN2	Cellular Communication Network factor 2
BV	Bone Volume
TV	Trabecular Volume
F-Actin	Filamentous Actin
Col-I	Collagen - I

CHAPTER ONE: INTRODUCTION

1.1 Motivation

Bone health is a key factor in maintaining an individual's health, especially as they age. Fractures, and poor bone health later in life can lead to a compromised immune system, inability to maintain exercise regimens, or difficulty in performing daily tasks[1,2]. A major biological element in maintaining bone health is the health of the marrow, and more specifically, the mesenchymal stem cells (MSCs) which reside within the marrow[3]. MSCs are progenitor cells for osteoblasts and osteocytes[2] which are responsible for bone deposition, and the internal mechanical signaling which directs osteoblasts, respectively[2,3]. Maintaining the health of these cells, then, is of critical importance for maintaining the health of bone structures[1-4].

The microenvironment, and microstrains inside of the marrow are key regulators of MSC activity[4]. MSCs have been shown to respond and differentiate in response to the stiffness of substrate[1,4], substrate induces strain[5-9], fluid shear[10-14], and vibration induced strain[15-20]. While this phenomenon is well understood, there is little to no understanding of what a biologiclly relevant strain looks like *in vivo*. This is, in part, due to the difficulty in accurately measuring the mechanical properties of bone marrow[21-24] which is a heterogeneous tissue that exhibits both elastic and fluid properties. This makes the pursuit of a biologically identical mechanical model for bone marrow incredibly difficult, and there is a severe need for a biologically relevant, reproducible mechanical model.

1.2 Research Goals

The first aim of this study is to create and validate a biologically similar 3D finite element model. The first goal of this investigation is to develop and validate a Finite Element (FE) model to simulate the mechanical strains experienced in an equivalent 3D printed synthetic model. Second, we aim to develop a model to mimic the structure, rheology, and kinetics of the trabecular structure within bone marrow. Third, we aim to analyze the mechanical behavior between a 13.5% and 25% bone volume scaffolds, to explore the role deterioration of the trabecular structure has on the mechanical environment.

The second aim of this study is to compare the cellular response in a 3D printable model. The first goal of this aim is to compare the cell behavior within the two separate bone volume scaffolds, 13.5% and 25%. The second goal is to correlate the behavior of MSCs in the synthetic model with the mechanical environment predicted by the FE model.

CHAPTER TWO: BACKGROUND

2.1 Mesenchymal Stem Cells

2.1.1 Overview

Mesenchymal Stem Cells (MSCs) are adult stromal nonhematopoitic cells characterized by their spindle shape and ability to adhere to polymer surfaces[3]. MSCs can be found in numerous tissues including umbilical cord, adipose, endometrium, and bone marrow. Their fame and focus of study derive from their ability to differentiate into osteogenic cells, osteoblasts and osteocytes, two key components to the bone regeneration cycle[2,3]. Besides osteogenic lineages, MSCs have been shown differentiate into chondrogenic, adipogenic, myogenic and neurogenic lineages. They also have been shown to be immune regulators by secreting cytokines and paracrine factors, in addition to regulation of the microenvironment[2].

The fate and function of MSCs has been shown to rely not only on chemical signaling between cells, but also through biophysical queues within the environment[1]. The stiffness of substrate on which the cell is cultured. For example, when cultured on a 2D substrate mimicking either neurogenic, myogenic, or osteogenic environments, MSCs saw a sharp increase in the corresponding phenotype of the substrate[1,4]. This behavior has also been shown to apply to both adipogenic and chondrogenic cell lines[4].

2.1.2 Mechanotransduction

Most eukaryotic cells are capable of detecting forces in their environment. This is critical to ensure homeostasis, by responding with the appropriate growth and development to maintain healthy tissue[25]. The transfer of these signals begins at the elastic cellular membrane, which is deformed and transfers this strain through the cytoskeleton, composed of large actin filaments, which connect to the nuclear membrane through the LINC complex[26]. The structure and density of the cytoskeleton combined with the stiffness of both the nuclear and cellular membranes combine to determine the mechanical structure of the cell[27]. Deformation in this system activates numerous biochemical signaling pathways, which has been the purview of many studies. Despite this, all of them have not been fully characterized, nor understood[1,4,27].

One such pathway, and a focus of this paper, is the Yes-associated Protein (YAP) pathway. Stimulation of Filamentous actin (F-Actin) during a deformation event, mechanically transduces YAP from within the cytoplasm, through the nuclear membrane, where it activates cell proliferation mechanisms[28]. This is not the only mechanism for YAP regulation, as the Hippo pathway also regulates proliferation including the accumulation of YAP in the nucleus[29]. YAP has been implicated as a regulator in the osteogenic line, and thus implicated in the mechanical regulation of osteogenic differentiation[30].

As previously mentioned, the stiffness of culture substrate contributes to the ultimate differentiation of MSCs[1,4], but substrate is not the only mechanical stimuli which can cause biomechanical responses. Substrate Strains (strains delivered via substrate)[25], and vibration[26,31] induced strain have also been shown to induce responses. Specifically,

osteogenic differentiation is caused during low intensity, high frequency vibrations (LIV). Generally, higher osteogenic differentiation is seen in the range of 10-800Hz, with the highest seen around 90-100Hz[32].

2.1.3 Osteogenesis

Osteogenesis is the line of MSCs differentiation during which Osteoblasts and Osteocytes are produced[33,34]. Differentiation to osteoblasts are broken up into 3 steps. The first is change into the osteoprogenitor. This phase is accompanied by an increase in alkaline phosphatase, and collagen isoforms, specifically precollagen and collagen-I[33]. Next, the osteoprogenitors become pre-osteoblasts. This stage is marked by the production of osteocalcin, osteopontin, bone sialoprotein and osteonectin[33]. Finally, the pre-osteoblasts become osteoblasts, which is marked by the production of hydroxyapatite[33,34].

2.2 Bone Marrow Environment

2.2.1 Overview

Bone marrow is a soft tissue in the central cavity of long bones and within the pores of trabecular bone[22]. It is divided into two main classifications: white and red marrow. White marrow tends to be in the cortical regions, while the trabecular regions of long bones have red marrow. The trabecular regions contain both the hematopoietic and MSCs[23]. The cells which comprise marrow are mechanosensitive, which are stimulated through normal kinesthetic motion. Vibrations are translated through the ankle, which results in 10-100hz vibrations in the femur[35]. Given that MSCs, hematopoietic and immune cells are located within the various regions of marrow, modelling the mechanical motions these cells experience is vital to our understanding of their continual health.

2.2.2 Material Characterization

      While the mechanisms of cell signaling within the bone are understood, the actual environment and magnitudes that MSCs experience are unknown[22]. A significant difficulty in mechanical modelling comes from the heterogeny of the material. Young's Moduli of 0.25-24.7kPa[36] and a viscosity of 37.5-1000 cP[37] have been reported. The variation seen has a variety of sources. Different methods of analysis are a major source of error. For instance, measuring the material conditions under pressure, as normal bone marrow is, can change the moduli and viscosity measurements by multiple multitudes[36,38,39]. Freezing the marrow for storage has been shown to show one magnitude lower viscosity when measured, likely from the disruption ice crystals had on the stability of the ECM[22]. Age and location of testing (red/white, cortical/trabecular, in bone/outside) can also affect the given results[38,39]. These factors limit the viability of studying biological models from a purely material characterization.

      In general, marrow behaves as a fluid at body temperature, and appropriate rheological measurements seem to have given us the most consistent results[37-39]. These measurements come with their own flaws, as all commercially available rheology machines require the removal of marrow from the bone, which can (and does) disturb the cellular environment[22]. Additionally, while the general behavior is that of a fluid, most of these measurements are performed outside of bone extracted via syringe; this neglects the elasticity of the extracellular matrix within bone marrow[22,38,39]. Not only does the syringe shear the elastic matrix, the rheology also shears away any structure that may have remained[37]. The elastic moduli have also been estimated using nanoindentation. Indentation comes with its own problems, as it has no method of characterizing shear

(and thus viscosity) of the tissue[37]. Given the known behavior of marrow, and from previous explorations of MSC behavior, the consensus[22,36,38,39] is that shear strain is the major component of mechanical stimulation *in vivo*, but this shear can have both elastic and viscous components.

2.2.3 Visco-Elastic Modeling

Generally, the stress-strain response of materials is divided into 3 categories: elastic, viscous, and visco-elastic[40]. Elastic materials are those that we classically consider for material modeling: steel, ceramics, some plastics. They are materials which have *in phase* stress-strain relationships. As you increase the strain/displacement on the material, you also increase the stress/force exerted by it. Viscous materials, on the other hand, have *out of phase* stress-strain relationships (one is the derivative of the other) and are classic fluids. As you apply strain/displacement to a viscous material, the stress/force exerted does not change, unless you change the rate of applied strain/displacement. Thus, they are a rate dependent material. As the name suggests, visco-elastic materials are a hybrid between elastic and viscous, exhibiting behaviors of both. Most biological tissues and soft polymers are classified as visco-elastic materials[40]. The structural behavior of biological materials pressures the molecular rearrangement of the tissue to continually balance between elastic and viscous behavior to maintain homeostasis.

Visco-elastic materials have time (and often temperature) dependent behavior. In short time periods, they behave similarly to elastic materials[40,41]. This allows the description of their behavior using common elastic modelling methods. However, unlike elastic materials, if held at a constant strain/stress will exhibit relaxation/creep respectively. In the case of constant strain, over long time periods the stress will decay

towards a value known as the long term moduli[40,41] which describes the relative viscous/elastic nature of a material. The closer it is relative to the instantaneous (short term) moduli, the more elastic the behavior. The time it requires to reach this long-term modulus is proportional to the viscosity[40,41] If a visco-elastic material is held at a constant stress, it will exhibit creep. As the material relaxes and loses elastic energy, the strain of the material will increase until failure, "creeping" across the test. It is important to note that creep can also occur in traditionally elastic materials, such as metals under high stress or high temperatures, glass, and lead.[40] Generally visco-elastic materials exhibit a much higher rate of creep (seconds or hours), than structural creep (years or decades).

The ideal method of modelling visco-elastic materials is using either Resonant Ultrasound Spectroscopy (RUS) or Broadband Viscoelastic Spectroscopy (BVS). These techniques use alternating excitation to obtain either frequency or temperature properties of a visco-elastic material[42]. This broad-spectrum analysis is incredibly useful for obtaining either full elastic tensors, or full spectrum temperature or frequency analysis using a single sample. Both, however, provide difficulties in measuring tissues taken from biological samples and extremely soft materials, because they both rely on the regularity of the sample in obtaining their data. This criterion makes them ineffective in modeling marrow and other biological until developed further[41,42].

When modelling visco-elastic parameters it is vital to acquire experimentally valid data. As these materials are highly sensitive to both frequency and temperature changes, modelling should match these values. As such, this study maintains the same rate of vibration when acquiring elastic descriptions and acquires data at the identical temperature.

2.3 3D Printing

2.3.1 Overview

3D printing has been a burgeoning technology for the past few decades. Rapid advancement in both fabrication and processing power have led to a flood of consumer affordable printers that can easily sit on a desk[43]. The ability to render digital designs quickly has given rise to rapid prototyping and new distribution avenues of goods. The economics of manufacturing one-of-a-kind items has fallen drastically, engorging digital small-business storefronts with items an individual can hold within hours[44]. This novel technology has also invaded biological study. Surgeons have used 3D printed implants for vertebral fusions[43], dentistry, maxillofacial surgery[44], surgical guides, and patient specific joints to improve patient[45] recovery are but a few applications

2.3.2 Biological Techniques

The two primary methods employed in biological 3D printing are FDM and SLS. Fused Deposition Modeling (FDM), is a technique reliant on adding layers of material (in most cases thermoplastics) to create a 3D structure. The types of materials used in FDM are incredibly broad, and most common materials have very advanced techniques for creating incredibly complex structures[44,46] In order to be used, a material must be extrudable, whether through heat or emulsion and to somehow fuse or adhere between layers[44]. This has been applied to plastics[43,44] (especially PLA and ABS), inorganic polymers[44-46], metals[43,44], wax[44], ceramics[43,44,46], and cells[46] to name a few. This broad range makes it an ideal candidate for a wide range of applications, especially sinter-able cancellous bone analogs[47-49] which serve as excellent mechanical representations for trabecular bone, usually being made out of hydroxyapatite[47,48] or α-tricalcium

phosphate[49] (a precursor for hydroxyapatite[48]). This flexibility does have downsides. The nature of FDM limits both the resolution and structures which can be generated. While both of these are incredibly material dependent (for instance thermoplastics have reported resolutions of 0.0005mm[43]), in general some of the more exotic materials and slurries are limited in their structure and composition[47].

Selective Laser Sintering (SLS) is a printing technique used exclusively for sinter-able materials (metal, ceramics) in which a high heat laser electively sinters a fine powder of the desired material in a layer-by-layer format. What this technique lacks in material breath it makes up for in accuracy and precision. The structures generated in SLS printing are limited only by the grain size of the material, and the size of the laser, making for incredibly fine structures[43,50].

FDM was selected for this study, for its reliability and flexibility. While this study is on the lower end of most conventional FDM printers' resolution, higher end printers are more than capable of creating structures of this size. Additionally, FDM is one of the more common forms of 3D printing, and this allows a greater reach for this model. Next, this study chose PLA for its material, as it is cheap, biocompatible, accurate, and easy to print with. These scaffolds were then combined with a cell seeded hyaluronic acid to create a biologically replicant model.

2.4 Digital Image Correlation

<u>2.4.1 Overview</u>

Digital Image Correlation (DIC) is a method of analysis utilizing a camera viewing a speckled surface, which is employed to measure full-field strains of the surface. This technique was developed by the University of South Carolina,[51] and has gained popularity in the mechanical modeling of biological tissues[52,53] because it can be applied to any material that has a random, imageable surface pattern, or can have one applied to it. The analysis works by dividing up a set image into discrete pixels subsets, which correspond to the surface pattern. The program then tracks these subsets as they move from image to image, and compare their position to where they started, generating the full-field strain values in each image from this displacement[51,52].

<u>2.4.2 Technique</u>

When interpreting in DIC analysis, it's important to plan for multiple factors. The subset size (the discreet size of each pixel grouping), determines the threshold a subset can move to be considered the same subset. Failure to choose the appropriate size will lead to the program mistaking one subset for another. Next, we have the strain radius. This value is used when correcting for high deformation subsets being next to smaller deformation subsets, by averaging between the two values[51]. Too large of a value can mute the responses of critical regions, too small can create excess noise that would otherwise be cleared out. A value twice that of the subset radius is recommended as a starting point before further refinement[51,52]. Lighting and contrast are also important to consider when analyzing. Surface glare can obscure the surface patterns and cause the program to "lose" a subset through the images. Likewise, a lack of contrast against the

background can prevent an accurate subdivision of the initial surface, inhibiting the tracking of the subsets over time. Finally, DIC is a method which is only valid in a 2D plane, and any out of plane changes will not be accounted in the strain field, and too large a change outside of the camera's field of view can invalidate subset tracking[51,52] This limitation can be reduced with a camera possessing a large field of view (FOV), however, as the FOV increases, there is a decrease in the resolution accuracy (and thus valid frame rate) of the camera measurement.

2.5 Finite Element Modeling

2.5.1 Overview

Finite Element (FE) modeling is a powerful technique used in a variety of mechanical applications to simulate the mechanical loading a geometry would experience during a set loading regimen[54]. The applications vary from quality control of a product, to optimization of geometries for research and design. While its application is varied, its premise is incredibly simple. By subdividing a geometry into discrete points, and setting the interactions between those points, a computer can perform a rigorous and thorough calculation for the mechanical loading each point, for each timeframe[54].

FE modeling's strength is that of versatility. While other characterization methods require exact characteristic equations for a given geometry to generate valid computations, FE modeling allows any geometry to be used and the upper limit is computing power. Provided an appropriate model and system is used, and those models are validated, this method is a useful tool to understanding the mechanical environments of biological tissues[55].

13

2.5.2 Previous Models

Previous attempts have been made to computationally model the bone marrow environment, each possessing limitations that we hope to improve upon. The first example involved the modeling of marrow as idealized cylinders, in an orthogonal organization[56]. Fluid was vibrated over the surface of the scaffold at frequencies ranging from 30-80Hz, and the surface shear which resulted was measured. The viscosity range tested was between 0.1 and 0.4 Pa s, 100-400 cP[56].
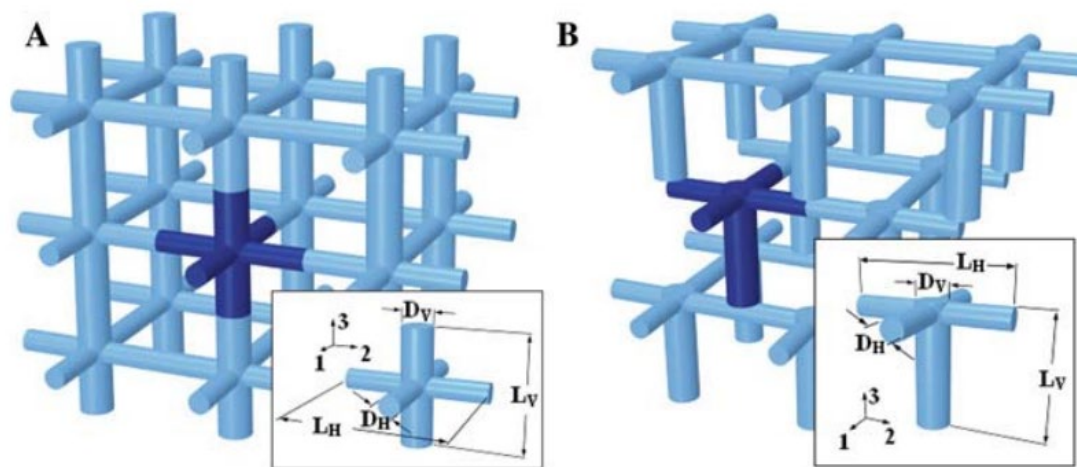
Picture 1.   Orthogonal computational model[57]

This model takes into account an idealized structure with biologically relevant geometries and material definitions to produce biologically relevant results. However, the idealized structure limits the applicability to a true biological structure. As a start, modeling trabecular structures as cylinders orthogonal to each other produces hard corners, which not only wouldn't be present in a biological system, but also can create errors in the finite modeling[58], which the authors recognize and thusly record values in the center of the cylinder surfaces[56]. Gyroids are generally the best accepted idealized

model; they are easy to fabricate via additive manufacturing, their fluid modeling

behavior eliminates corners, and they provide a large surface area for cells to adhere[58].

Another model aims to create a biologically relevant structure, not just sizes and

values[59]. This was done using μCT scans of trabecular bone in a vertebra imported into

an FE modelling software. Both the bone and marrow (which here is referred to only as

fat cells), were modelled using previous studies' experimentally derived Young's Moduli.

The loading was a continuous load, which they explored between 500 and 1200N.

Additionally, both the bone and marrow's moduli were assumed to be linearly elastic[59].
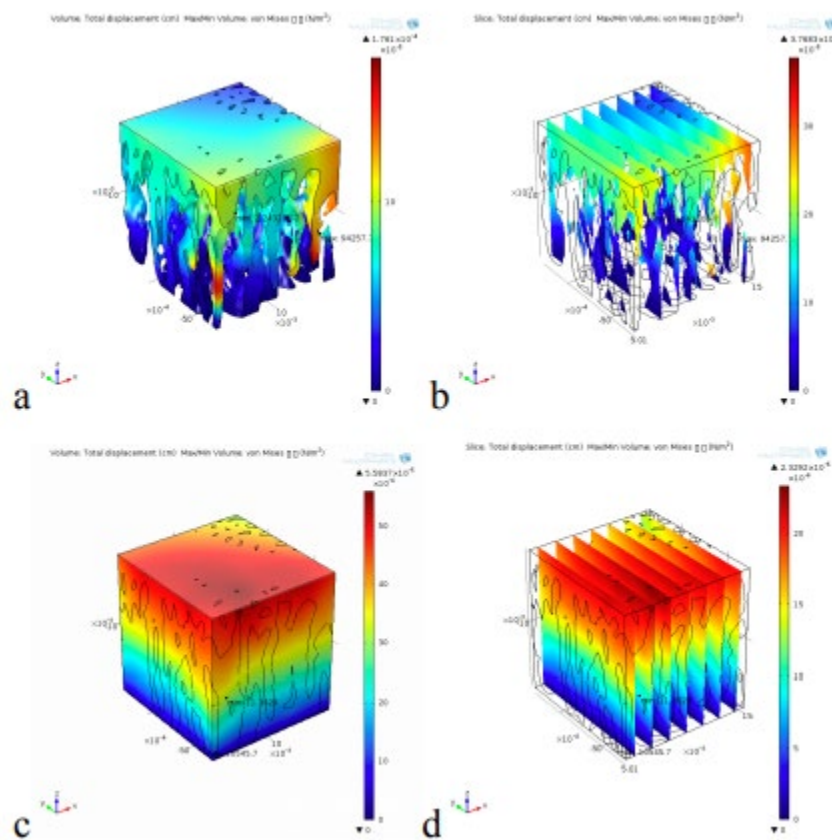
Picture 2.   Biologically identical, mechanically idealized model[59]

While this model uses biologically derived geometries, the modelling of the marrow, it doesn't accurately capture the behavior of mechanical loading. First, most sources agree that marrow either exhibits mostly viscous, or visco-elastic [22,36,38,39,56] so modelling it as linear elastic (which is itself disputed[38,39]) provides no biological relevance. Second, the loading is not dynamic, and a constant stress on the bone isn't accurate to the expected loading within a trabecular structure[32,39,56]. So, while this model is a step up in geometry, it's a step down in bio-mimetic material values.

The final model presents us with a mixture of biologically derived geometries and biomimetic mechanical values[39]. Here, μCT scans of a human's trabecular regions in various bones are used as the geometric basis for a computational fluid dynamics model. Here they homogenize cell to cell interactions, and assume that marrow is a homogeneous viscous fluid, and apply between 10 and 90Hz, 1g amplitude fluid force across the structure. The full field 3D shear stress was examined throughout the bone.
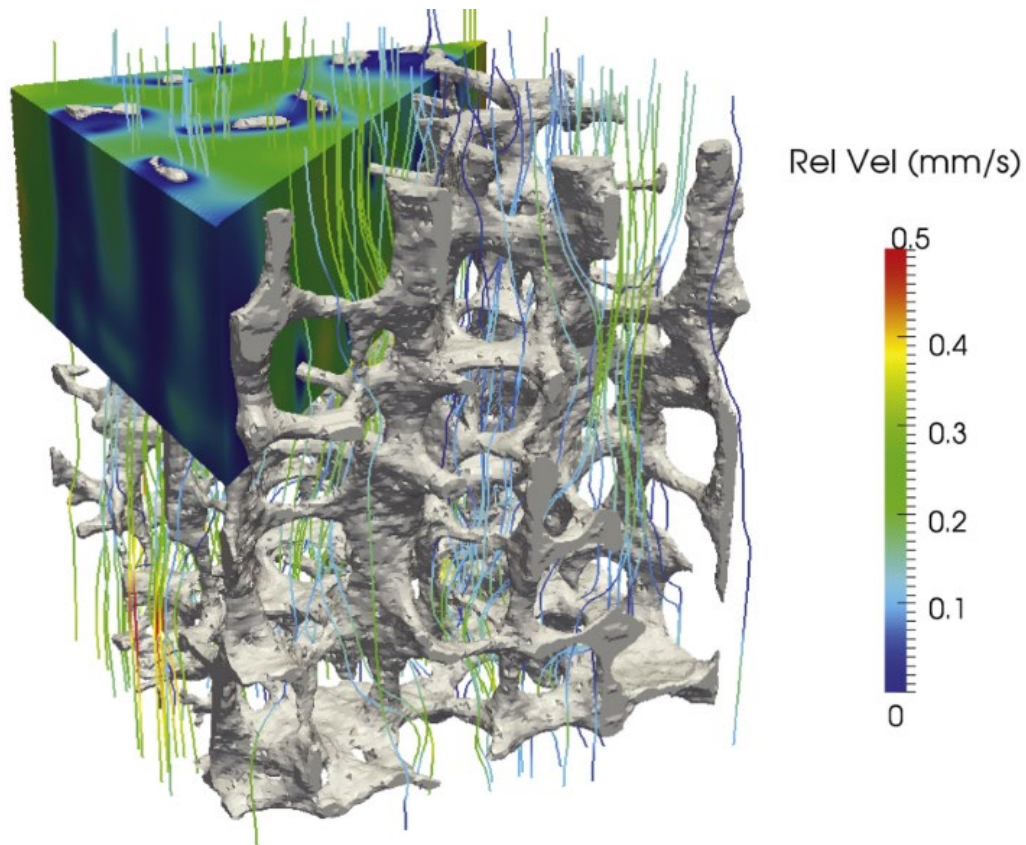
Picture 3.   Biologically relevant structure and mechanical model[21]

This model provides an example of a biologically relevant simulation, taking

some liberties with assumptions (like a homogeneous viscous fluid), but overall creates a

mimetic simulation. However, like all the previous models examined, has no way of

experimentally validating that their model is correct. The viscosity is taken from

previously examined bone marrow, but we have already examined why those

homogeneous viscosity values are often incorrect, or highly variable[38,39]. Furthermore,

there is no way to correlate these values to a biological system's behavior, as it is

impossible to measure marrow mechanical properties non-invasively[36,38]. This prevents

any studies examining the role that bone geometries, material properties, and

environments affect the behavior of MSCs.

CHAPTER THREE: MANUSCRIPT

1. Introduction

Mesenchymal Stem Cells (MSCs) in the bone marrow are regulated by mechanical stimulation both *in vivo* and *in vitro*[1,2] . While *in vitro* studies have the advantage of precisely applying forces and measuring the response[1,4], quantifying the cell mechanical environment *in vivo* is challenging and thus limiting the ability to understand the components of mechanical signals that drive cellular response. Therefore, development of computational models - in combination with *ex vivo* or tissue-engineering models - that can capture the mechanical and geometrical complexity of bone marrow MSCs environments will be critical in mechanistic approaches to understand the mechanical factors that drive MSC mechanoresponse at the cellular level.

Inside the bone marrow, bone surfaces where bone cells reside, are exposed to matrix deformations[5-9], accelerations[15-20], fluid flow[10-14], and changes in intramedullary pressure[60-62], all of which are inseparable[63]. During strenuous physical activity the bone strains can reach up to 2,000–3,500 microstrains ($\mu\varepsilon$)[6]. During these cyclic bone deformations cells embedded within bone matrix are also subjected to fluid flow with 400 $\mu\varepsilon$ strain magnitudes associated with activities such as walking, which generate fluid velocities up to 100 μm/s within the lacunar–canalicular network [64]. Cells that reside on or in proximity to bone surfaces also experience fluid flow. This flow is relative to the marrow's relative motion to the bone surface. For example, tibial accelerations reach up to 2g (1g corresponds to 9.81 m/s^2 - Earth's gravitational pull) during moderate

running[65], which can drive these marrow-bone interactions. Bone also experiences a barrage of smaller strains. 24 hour strain history across different species showed that large strains (> 1000 µε) were infrequent while very small strains (< 10 µε) were recorded to happen thousands of times a day, suggesting that small magnitude events are physiologically relevant [66]. Leveraging the presence of these small strains, application of low intensity vibration (LIV), usually applied between 30 and 100Hz with acceleration magnitudes ranging from 0.1 to 1g, have been utilized in clinical, pre-clinical and cellular studies[67]. In clinical studies, LIV protects bone quantity and quality in women with osteoporosis[68,69], children with cerebral palsy[70], and improves bone indices in child cancer survivors[71]. Animal studies demonstrate that external LIV application increases trabecular bone density and volume[15], results in stiffer bones [72], and impedes the disuse-induced bone loss[73].

At the cellular level, using both horizontal and vertical LIV systems, our group has reported that application of LIV increases MSC contractility [74], activates RhoA signaling [24], and results in increased osteogenic differentiation, as well as increased proliferation of MSCs[75]. Similar to other mechanical signals such as substrate strain, LIV increases the nuclear accumulation of β-catenin[76] and YAP[77] that act as mechanically-sensitive transcription factors to increase cell proliferation as well as directly affecting heterochromatin compaction to increase nuclear stiffness[78]. We have recently reported that in a simulated microgravity model where MSCs were exposed to rotating cell culture vessels for 72h to simulate gravitational unloading, LIV was able to rescue reduced cell proliferation[79] and YAP nuclear entry induced by RhoA-activator Lysophosphohaditic acid[77].

Despite the effectiveness of LIV at tissue and cell level, the mechanical environment LIV generates within the bone marrow cavity is not well studied due to a lack of easy to use and repeatable model systems that can replicate the mechanical complexity of the bone marrow pores during LIV stimulation. Previous *ex vivo* models have been developed to model the mechanical environment of trabecular mechanical environments. For example, modeling small cancellous bone strains generated by LIV using a rectangular –idealized bone lattice reported that surface strains up to $15\mu\varepsilon$ can generate fluid shear stress on bone surfaces up to 2Pa depending on the bone marrow viscosity[57]. Another study utilized realistic bone geometries from μCT scans of a human lumbar vertebra to model the fluid shear-stress at trabecular surfaces during LIV[21]. Follow-up studies that combined the computational modeling with trabecular explant models under LIV showed that while LIV-induced fluid shear correlated with histological findings that fluid shear alone was not able to explain the response as the response measured at fluid shear only groups remained lower than the LIV groups[80]. While these models provide insight into possible mechanisms, biological variation and sample availability makes it challenging to setup studies with multiple outcomes from identical conditions. Another challenge is the characterization of the bone marrow. For example, age and location of testing affect the given results and are hard to control for[3-7]. Furthermore, while these studies have elucidated the role of fluid shear, strain, and acceleration on determining MSC fate and function, these value's relation to different trabecular geometries has not been able to be examined. This limits the ability to create generalized conclusions about the behavior of trabecular mechanical environments. In human and animal models, changes to the trabecular density occur with both age[8,9] and

different exercise levels[10,11], necessitating a model which can explore the implications of these changes in a mechanical environment.

Towards these ends, we have selected two different bone volumes to compare mechanically, 13.5% and 25% idealized gyroid structures. These are biologically equivalent to a 64 week and 8 week old adult male mouse.[81] This allows us to model the mechanical environment of the trabecular structure and how it changes the strains experienced by MSCs.

In order to generate a repeatable model for studying the changes in bone density under LIV, we have developed a cell-laden bone marrow analog with a 3D printed, PLA based trabeculae and hyaluronic acid hydrogel based bone marrow to quantitively measure the effects of trabecular volume on MSC response during LIV. The strains created during 1g, 100Hz vibrations in both 13.5% and 25% trabeculae bone volumes were compared via both a validated finite element model and using fabricated *in vitro experiments* to study if the trabecular bone volume affects the bone mechanical environment.

Experimental Design

To create a validated experimental bone-analog model, PLA was chosen for the material of the trabecular structure due to its biocompatibility[82] and ease of use in 3D printing applications[43]. Previously developed custom-made hyaluronic acid-based hydrogels with MMP cleavable and cell attachment sites were chosen to model bone marrow[83]. Primary mouse MSCs dispersed in hydrogels were used as the cell model due to their versatility in both proliferative and differentiation experiments utilized in previous studies[5,6,15,24,72,73,75-77,79]. In order to generate an experimentally validated finite

element model, two different hydrogels were used. One, a collagen-based gelatin hydrogel (will be referred to as calibration gels) was used to calibrate the model as a cost-effective material. Hyaluronic acid hydrogels, which will be the focus of the cellular aspect of the study were the secondary hydrogel used following the established procedures created with the calibration gel. Following the model validation via calibration gels, key validation experiments were repeated using hyaluronic acid hydrogels to generate material specific information. Due to large difference in elastic modulus[36,37,82], PLA scaffolds were assumed to be rigid for the purposes of the finite element (FE) model. To replicate hydrogel material properties for the finite element model, we first employed a high speed compression test to measure the instantaneous elastic modulus over a time period similar to the vibrating frequency (100Hz), and a second 100 second relaxation test to measure the viscous response. Hydrogel response to 1g, 100Hz vibrations were experimentally measured in wells with variable widths (3-8mm) via high speed speckle photography using digital image correlation (DIC) analysis. Resultant LIV-induced strains were used to calibrate and validate the FE model. Friction and damping boundary conditions between the PLA and hydrogel was found by empirically minimizing the root mean squared error (RMSE) between experimental and FE-based surface strain fields. Identical validation steps were followed for hyaluronic acid hydrogel using only the 8mm spacing model. Following the FE model validation, idealized 3D trabecular structures based on gyroid models[17] with either 13.5% or 25% volume fill (i.e. trabecular volume) were generated and LIV-induced hydrogels strains were compared using the respective FE models.

For *in vitro* experiments, two sets of PLA scaffolds (13.5% and 25% volume fill) were fabricated from idealized gyroid based 3D trabecular models using a PRUSA Mk3s 3D printer (PRI-MK3S-KIT-ORG-PEI) with 0.1 mm layer height, and 0.5 x 0.5 x 1 cm overall outer dimensions. These scaffolds were Ethylene oxide-sterilized and shipped to collaborators to fill with hydrogel-encapsulated MSCs at 1 million cells per mL of hydrogel. Hyaluronic acid-based hydrogels were crosslinked with poly(ethylene) glycol-modified peptides: GRGDS and metalloproteinase-labile peptide 'PQ.' Crosslinking density (3:1, thiol:acrylate) was used where thiol-functionalized hyaluronic-acid and acrylated peptides were incorporated. Cell-laden hydrogels with no PLA scaffold were used as negative controls (referred as 0%). Throughout the experiments, samples were kept under growth media (IMDM, 10% FCS and 1% Pen-strep) and changed every 7 days. Cell-laden 13.5 and 25% scaffolds were either vibrated one hour every day at room temperature using 100 Hz frequency and 1 g acceleration magnitude or kept outside of the incubator for 1h/day but not vibrated (N=8 scaffolds/grp). 0% scaffold-less controls were treated the same as non-vibrated control groups (N=7 gels). After 14 days, samples were allocated for mRNA (N=4 scaffolds/grp), immunostaining (N=3 scaffolds/grp) and acute-LIV outcome (N=1 scaffold/group). For acute-LIV outcome, we have employed a recently developed immunostaining protocol to measure LIV-induced nuclear YAP entry[31]. Four total scaffolds from non-LIV controls (two 13.5% and two 25%), were assigned to either control or acute LIV. Acute LIV groups were vibrated 5 times for 20 mins each with one-hour rest between sessions. Controls were handled the same but were not vibrated. All the experiments were repeated three times except for the qPCR outcome which was only repeated twice.

2. Methods and Materials

Preparation of Hydrogels

Mechanical tests were performed using either collagen-based calibration gels (Knox

unflavored Gelatin) or hyaluronic acid (HA) hydrogels that we used for quantifying *in*

vitro experiments (Advanced Biomatrix: GS1004). The manufacturer reports a free

diffusion of particles less than 75 kDa, with pore sizes of 17 nm. Samples were prepared

in 3D PLA printed cylindrical molds with a diameter of 24 mm and a height of 9 mm

(Figure 1c). The calibration gels made from a mixture of collagen I-III were prepared at 2

mg/ml via dissolving the gelatin powder in 50ºC water. Sample molds used for

calibration gels were lined with a thin layer of petroleum jelly to improve mold release

and 4.1 ml of 2 mg/ml gelatin mixture was pipetted in. Filled molds were cooled over ice

for 1 hour, to cross-link, and then both the gel and mold were deposited into a room

temperature water bath to for 30 minutes. The calibration gel samples were carefully

removed from the molds and tested. All tests were completed within 3 hours of initial

calibration gel deposition into the molds (Figure 1a). Hyaluronic acid gels were prepared

according to manufacturer protocols[13]. Briefly, degassed (DG) water was extracted via

syringe and added to the Glycosil (5.0 ml DG water) and Extralink-Lite (2.5 ml DG

water). These were vortexed on a rocker for 60 minutes, with vigorous vertexing by hand

every 15 minutes. These solutions were then combined in a 4:1 ratio (v/v) (Glycosil to

Extralink-Lite) and mixed by pipette into the mold/well. These gels cross-linked for 90

minutes at room temperature, removed from the mold, deposited into PBS in 90mm well

plate (VWR#10062-878) sealed with parafilm, and left overnight in a 37°C in an

incubator, and. The next day the gels were tested one at a time, removing them from the PBS immediately prior to testing.

Instantaneous Compression Testing

Instantaneous compression testing was performed on an INSTRON ElectroPuls E10000 using a 10N load-cell attached to a loading plated with a diameter of 35mm. At the start of each test, calibration and HA gels were placed on water-coated Teflon sheets to prevent adherence (Figure 1f). The samples were pre-loaded with 0.025N to ensure full contact with the plate, then compressed to 20% strain (compared to pre-loaded gauge length) at a rate of 90 mm/s. Loading platen position was then held constant for 100 seconds and load-cell data was collected and exported into an excel sheet. Force and displacement data was collected during 20% compression, then input into Matlab, converted to stress and strain, and then fit using a 5th order polynomial $[f(x) = ax^5 + bx^4 + cx^3 + dx^2 + ex + f]$ (Figure 1e). The 100 second relaxation data was fitted using a 2-term exponential decay function $[f(x) = ae^{bx} + ce^{dx}]$. These 5th order polynomials representing the instantaneous material behavior and 2-term exponential decay functions representing viscoelastic material relaxation were averaged over three independent experiments. During analysis of calibration gels, it was discovered that the prolonged stay at room temperature had stiffened the calibration gel's modulus (see Supplementary Figure S1, which were outside of the 3 hour mark in which all DIC testing was performed (Figure 1a). To avoid modeling stiffer gel behavior, we have only used the original values for the samples that were tested within 3h. For the data collected beyond 3h, the average of maximum stresses were normalized to the average of the mean stress of samples that were tested within 3h (Figure 1e).

DIC Vibration Testing

Prepared calibration gels were tested in wells with differing width for validating the finite element model. The wells with fixed depth (9mm) and height (27.5mm) were 3D printed out of PLA for widths of 4mm, 5mm, 6mm, and 8mm (Figure 3a). These wells were filled with calibration gels as described above and were then speckled with a 50/50 mixture of talc powder and 220 SiC to track their motions via speckle photometry as previously described[18]. In order to track light-reflective speckles, a white LED light source was used and the motion of the surface was captured with a Photron UX50 high speed camera at a rate of 2000 frames per second (fps). PLA wells filled with calibration gels were vibrated horizontally at 100Hz with an acceleration of 1G via a custom-made vibration bioreactor driven by a Labworks ET-126HF-1,-4 (13lbf) Electrodynamic transducer using a sinusoidal driving function (Figure 1b). All the vibrations were performed within 3h of gel casting. Recording of gels sample motion was started 15 seconds after the start of vibration to ensure that steady state was reached. Recorded high speed videos at 2000fps were analyzed using digital image correlation (DIC) with NCORR software[84] (V1.2) in order to export relative gel displacements relative to a moving frame of reference marked on the well surface (Figure 2a). Post-processing of the full-field displacement maps were performed in MATLAB using a custom-made code. Vibrations were applied along the variable width of the well. For clarity, vibration direction is referred as x-direction and the well height direction is referred as y-direction. During the post-processing of the vibration experiments, the ε_{xx} strain was exclusively analyzed, as it was found to be at least one order of magnitude larger than ε_{yy} or ε_{xy} (see Figure S2). Given the imprecise methods in creating regions in NCORR, there was

variability in the size of regions. In order to average them, the center of each of the three regions (as seen in Figure 2a) was found, then the outside was trimmed to the size of the smallest region. They were then averaged at the $\pi/2$ and $3\pi/4$ time points (Figure 2b), reversing the latter to match the former, in order to capture peak strain values for each sample set. For HA gel experiments, only the 8mm well width was used and same steps were repeated as above. All the experiments were performed in triplicate.

Finite Element Model Generation and Validation

An *Altair Hypermesh v2017.2* software package was used to generate the finite element model. The hydrogel's bone wells were imported as .stl files and converted to rigid R3D4 mixed elements with a size between 0.5- and 10-mm. The hydrogels were meshed using square C3D8R elements with a size of 0.25 mm. C3D8R elements were chosen to prevent hour-glassing sometimes expressed with other element types. These hypermesh models were then used in *ABAQUS (R2019x, Simula, RI)* to simulate vibration. The hydrogel material was modelled with a density of 1.0023 g/cm^3 for calibration gels and a density of 1.0018 g/cm^3 for HA gels. Viscoelastic and hyperelastic material responses were modeled using the procedure outlined by Dalrymple[12]. For viscoelastic modeling, the long-term relaxation was measured starting from the end of the instantaneous compression to a 100 second interval (Figure 1d). This was then fit using a second order exponential function, and data was extrapolated back to 10^{-4} seconds to ensure that ABAQUS was fed data within the rate of vibration (100hz). This data set was Normalized to the initial stress value and input into ABAQUS as a time-dependent normalized bulk shear moduli. The elastic material definition was modeled as hyperelastic with a 5th order Ogden fit, $U = \sum_{i=1}^{N} \frac{2\mu_i}{\alpha_i^2} \left(\lambda_1^{-\alpha_i} + \lambda_2^{-\alpha_i} + \lambda_3^{-\alpha_i} + \lambda_4^{-\alpha_i} + \right.$

$\lambda_5^{-\alpha_i} - 5) + \sum_{i=1}^{N} \frac{1}{D_i} (J^{el} - 1)^{2i}$ where λ_i are principal stretches, N is a parameter (in this

case equal to 5), μ_i, α_i, and D_i are temperature dependent material parameters. Using the

instantaneous, uniaxial test data (Figure 1e), these material definitions were created in

ABAQUS.

The material interaction between the undeformable and hydrogel parts used a

linear press-overclosure with a slope of $1.0\text{x}10^{-2}$ and a friction and damping coefficients

that minimized the difference between experimental and numerical ε_{xx} strain magnitudes

at timepoint $\pi/2$ using a design of experiments optimization as described below.

Mechanical vibration was applied using a connector actuator driven by a periodic

velocity equation with an amplitude of 15.61 m/s, and a circular frequency of 100 Hz

(628.31 radians). These values were derived to best match those experienced by the DIC

experimental data of 1G, 100Hz. Acceleration driven amplitude was initially used to

model the vibration, however linear drift occurred over time, and velocity was derived

from constitutive kinetic equations of motion, $x(t) = -\frac{B}{\omega} cos(\omega t)$, and $x(t) =$

$-\frac{C}{\omega^2} sin(\omega t)$, where x(t) is the displacement over time, ω is the frequency in radians, B

is the velocity amplitude and C is the acceleration amplitude.

Damping and Friction Coefficient Optimization

Data output of ABAQUS was extracted with python and processed in MATLAB.

The time dependent output was analyzed identically to the DIC experimental data using

RMSE comparison of the ε_{xx} surface strain at the $\pi/2$ timepoint using the 8mm well

width. To optimize the friction and damping coefficients of the wall-gel interaction in

the finite element simulation (of both the calibration and the HA gels), a 3 factor 3 level

design of experiments (DOE) was performed, using the default values of 0.75 and 0.03

for the friction and damping coefficients, the ABAQUS recommended defaults. The high

and low levels were one order of magnitude larger and smaller than the default values

resulting in total of 27 simulations (Table 1). This data, the calibration gel/hyaluronic

acid, was then compared against the experimental findings of their respective gel. For

each comparison, the experimental and computational full field ε_{xx} strains over the gel

surface of was divided into a 15x37 grid and the RMSE difference on each sub-region

were compared to each other to generate an empirical 2nd order polynomial, with

parameters. For both calibration gels and HA gels the friction and damping coefficients

that minimized the RMSE response was selected.

Scaffold Finite Element Modeling

Scaffolds were generated using two percent bone volumes, 13.5% and 25%.

These correspond to aged mouse bones and healthy adult male mouse bones,

respectively[81]. Gyroids were generated using the equation: $sin(x)cos(y) +$

$sin(y)cos(z) + sin(z)cos(x) < t$, where t is a constant linearly related to the percent

volume[17]. For 13.5% and 25%, the t scaling value used was -0.121 and -0.752,

respectively. These models were generated using *MathMod v8.0*, meshed in *Adobe*

MeshMixer v3.5 using a cell surface density of 128. The models were then scaled to

10mm^3 and cut into quarters, 5mm x 5mm x 10mm final dimensions. These were then

exported to *Altair Hypermesh v2017.2,* where the STL models were meshed using mixed

elements with an element size of 10mm (0.14mm after scaling). The meshes were made

into solid C3D4 elements using tetramesh and scaled to 10mm size. The bone geometry

was modeled using the surface face elements, and all but the gyroidal geometry

removed, creating a rigid R3D3 surface (Figures 4a and 4b). The final model was exported as an ABAQUS explicit input file.

The FE model was simulated in *ABAQUS (R2019x, Simula, RI)*. Pressure-overclosure with a slope of 1.0×10^{-2} was applied to ensure contact between the two surfaces, and both the surface damping and friction coefficients were taken from the optimization procedures. Similar to the previous simulations, the rigid bone was driven by a connector actuator using a periodic velocity equation with an amplitude of 15.61 m/s, and a circular frequency of 100 Hz (628.31 radians). The 13.5% and 25% scaffolds full strain profiles (ε_{xx}, ε_{yy}, ε_{zz}, ε_{xy}, ε_{yz}, ε_{zx}) were exported using a python script, and plotted into a histogram using MATLAB.

Scaffold Fabrication and Vibration

STL files of the 13.5 and 25% gyroidal scaffolds were 3D printed using PLA on a PRUSA Mk3s 3D printer (PRI-MK3S-KIT-ORG-PEI) with .1mm layer height, and 0.5 x0.5 x1cm overall outer dimensions. These scaffolds were sterilized with Ethylene oxide autoclave and shipped to UTHealth School of Dentistry for cellular encapsulation.

Scaffolds were flushed with an MSC-hydrogel mixture. HA is integrated with integrin binding motifs (acrylate-PEG-GRGDS) and metalloproteinases (MMPs)-sensitive peptides (PEG-PQ-PEG-acrylate) to encourage adhesion. Cells were seeded into the hydrogel at 1×10^6 cells/mL prior to cross linking. Cell seeded hydrogels were kept for 7 days in growth media in appropriate humidity, temperature and 5% CO2 to allow growth and attachment prior to experimentation.

Scaffolds were received and transferred to two 6 well plates (Corning#3516) with Growth Media (IMDM, 10%FCS and 1% Pen-strep). Scaffolds were oriented identically

to the 3D print, and with the long axis orthogonal to the axis of vibration. Scaffolds were secured with a custom 3D printed PLA top, and one 3D printed PLA 30mm platen in each well attached to a stainless-steel screw (Figure 1g) which was threaded through the top. These ensured the scaffolds would not move during vibration. The scaffolds were rested 24 hours after reception and then vibrated for one hour each day, for 14 days. Media was changed on day 8.

<u>Immunostaining</u>

Samples were rinsed twice in PBS fixed using 4% paraformaldehyde for 15 minutes at room temperature. Next, they were rinsed 2 times for 5 mins in PBS before being permeabilized in 0.1% triton/PBS for 15 mins at RT. All further steps have a 3x10 minute rinse in PBS between them. The scaffolds were separated further to be stained with four different antibodies: YAP, Paxillin, Collagen-I and Ki67. The four scaffolds from group one was stained for YAP. They were blocked using goat serum [*Jackson ImmunoResearch 005-000-121*] for 30 mins at RT, stained with *[Cell Signaling Technology# 14074S]* primary antibody for 69 mins at 37° C, and finally with goat anti rabbit [*Fisher Scientific A11037*] for 30 mins at RT. The next 3 stains had 5 scaffolds in each group. One each 13.5% and 25% vibrated, and one each 0%, 13.5% and 25% from the control group. Paxillin was blocked using [*Jackson ImmunoResearch 005-000-121]* for 30 mins at RT, stained with [*Cell Signaling Technology#12065S*] primary antibody for 60 mins at 37° C, and finally with [*Fisher Scientific A11037*] for 30 mins at RT. Collagen-I was stained using [*Bioss Antibodies#bs-10423R-A594*] for 60 minutes. The Yap, Paxillin and Collagen-I groups were then all Phallodin Stained [1:60 in PBS *Alexa Fluor® 488 Phalloidin- Invitrogen,cat# A12379*] for 60 mins at RT. The Ki-67 was

stained using [KI67 Conjugated Antibody] for 60 minutes, and then all samples (Ki-67, Yap, Collagen-I and Paxillin) were stained with NucBlue [Fisher Scientific#R37605] at 2 drops/ml. After a final two rinses for five minutes each, the scaffolds were imaged in PBS. Imaging was performed using A1R/MP+ Confonfocal/Multiphoton Microscope (Nikon Instruments) to scan the scaffold at a single cell resolution. Genes of interest were quantified and compared between LIV and non-LIV groups.

RNA and PCR

Each scaffold was centrifuged at 3000 rpm to separate the gel and scaffolds. Two gels were added to a single 2 ml tube, and TRIzol™ [*Fisher Scientific#15-596-026*] was added. They were mechanically broken up for 30 seconds with a P1000 micropipette. The rest of the extraction was performed according to the *RNeasy mini Kit 74104* protocol. The scaffolds which had been spun to remove the gel were suspended in Zymo lysis buffer and frozen at -80° C overnight. The RNA was then extracted according to [Zymo Research#R2071] and combined with the RNA extracted from the gel.

These RNA samples were then processed according to [SkanIt RE 4.1] protocols. These were then cycled at 95° C for 40 cycles in a thermocycler. PCR analysis was performed for Collagen-I using 18s as the control gene.
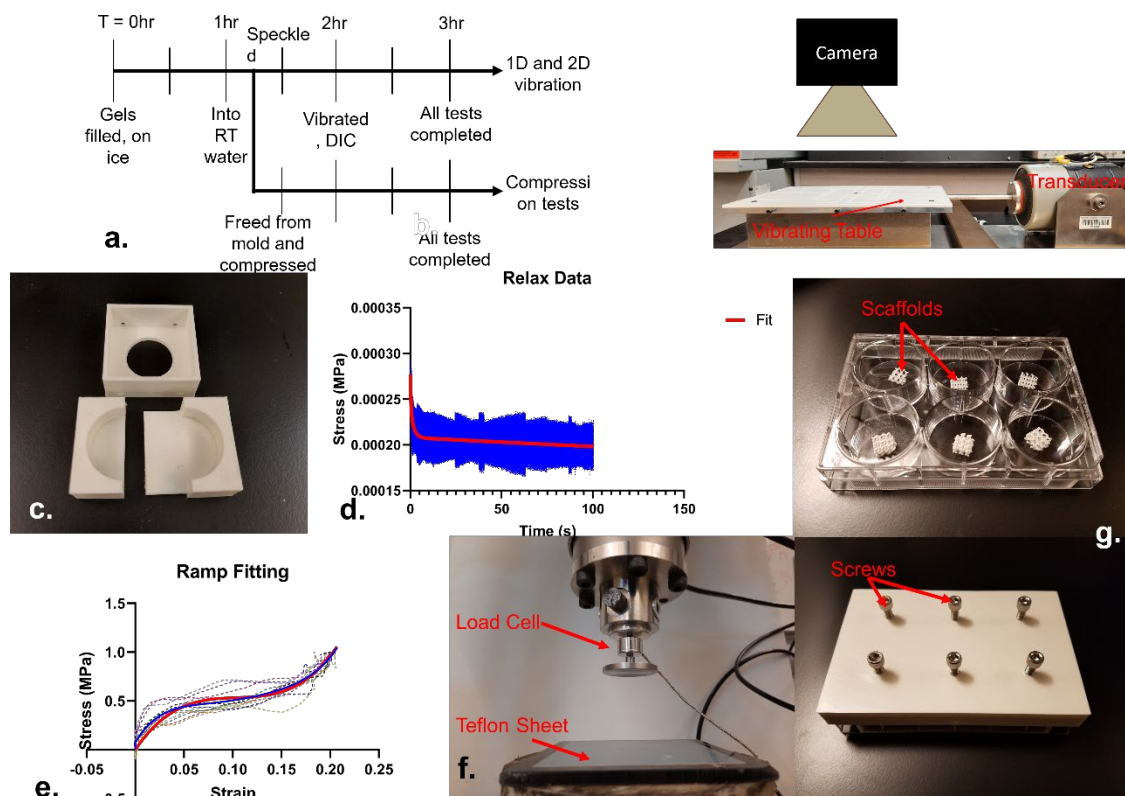
Figure 1. **Mechanical Experimental Setup. a) Timeline of the vibration and compression testing, with all tests completed within 3 hours of initial gelation. b) Setup of horizontal vibration plate (0Hz-2000Hz, 0.1-10g) driven by Labworks ET-126HF-1,-4 (13lbf) Electrodynamic transducer c) 3 Part 3D printed mold used to cast instantaneous gel pucks (24mm internal diameter, and a height of 9mm) d) Relaxation data over a 100 second time period (blue) and the resulting fit line (red) relaxing from 2.8e-5 MPa and reaching long term relaxation at approximately 2.1e-5 Mpa e) Normalized Instantaneous ramp data from 12 trials (dotted 5th order polynomial fit (blue), compressed to 0.2 strain (10.8 mm/s). f) Instantaneous compression setup, INSTRON ElectroPuls E10000 using a 10N load-cell. The sample was resting on a Teflon coated sheet lightly coated in water to prevent adherence. Image captured prior to measurements g) Custom 3D printed 6 well top to keep scaffolds in place during vibration**

3. Results

Lateral Strain positively correlates with distance during low intensity vibration

High speed visualization of horizontally vibrating wells at 100Hz frequency and 1G acceleration magnitude showed that the maximum lateral ε_{xx} strain, measured at the peak of the cycle (t= $\pi/2$ & t=3π/4), reached to 0.014±0.00047 at 8mm spacing over 5

cycles when averaged across three experiments (Figure 2b). The maximum ε_{xx} values were symmetrical on both ends of the well, ensuring that steady state was achieved during measurements. Measuring the averaged ε_{xx} distribution at positive and negative peaks, 34% of the total measured 1200 data points were between 0.015 and 0.013(Supplementary Figure S3a). Minimum strains were measured at the end of each positive stroke (t= π). While the average maximum values at t= π reached to 0.0035±0.000027, quantifying the distribution of average maximums across all measured samples showed that these values only corresponded to 4% of the total number of data points measured at t= π (Supplementary Figure S3b). The $\pi/2$ sets for each spacing over all three trials were collated into data distribution plots (Figure 2c). We can see a large difference in extrema from 4 to 5mm, and then a decrease in change from 5 to 6 and 8mm. Compared to 8mm at $\pi/2$ & t=$3\pi/4$ timepoints, averaged maximum ε_{xx} strains of 6mm, 5mm, 4mm well widths were decreased to 0.00806±0.00050 (-0.86%, p=0.66), 0.0075±0.00047 (-7.6%, p=0.17), 0.0030±0.00014 (-62%, p<0.05) , respectively. Shown in Fig.2d, quantifying the strain profiles over the half-width of each well showed a non-linear relationship between ε_{xx} strains and X- distance. ε_{xx} strains at 8mm at the wall2e – dotted red line).
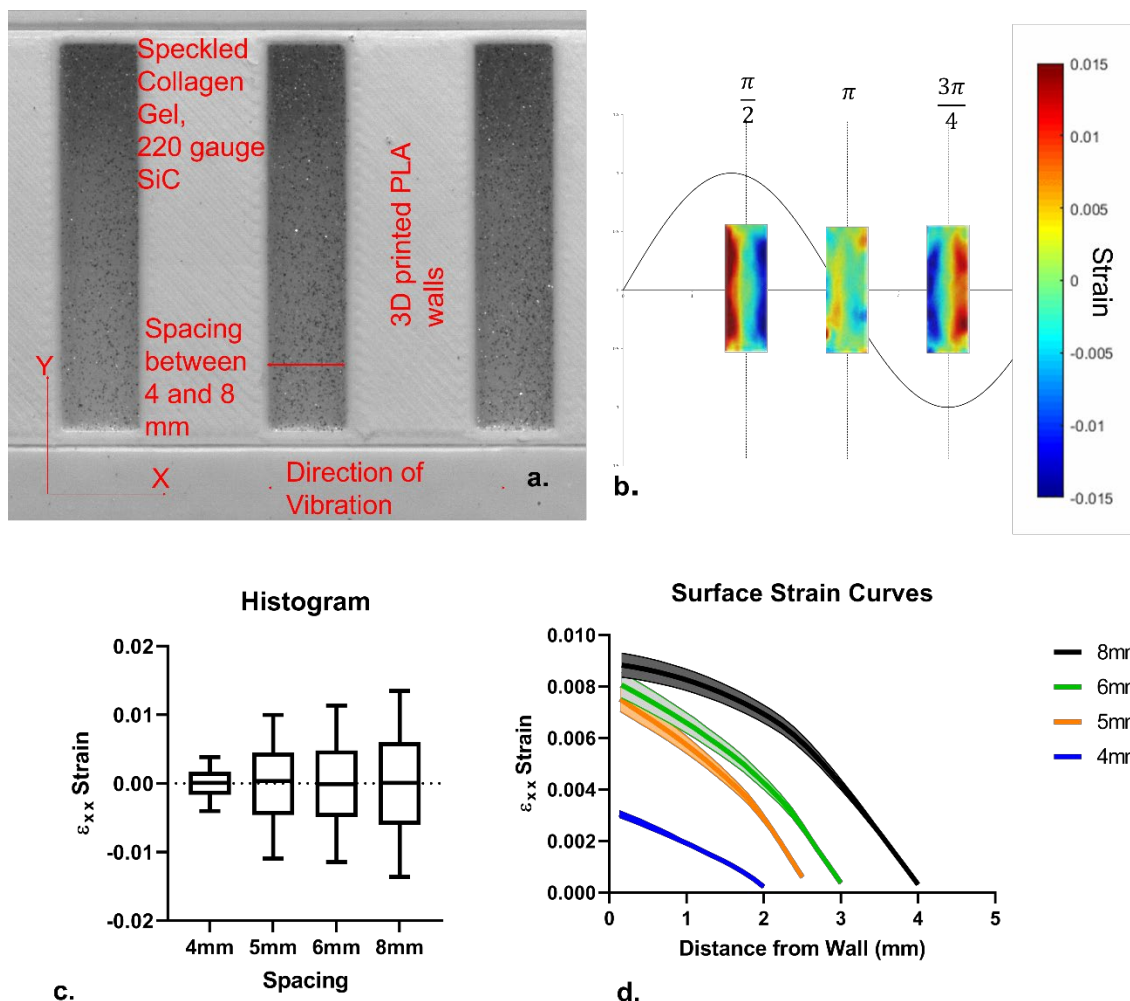
Figure 2 **a) A PLA experimental setup was manufactured to visualize strain during100Hz -1g vibrations at the horizontal direction. Hydrogels were speckle with 220 SiC and the camera recorded the motions at 2000 frames per second (fps) b) εxx strains varied periodically with the maximum value of 0.015 at 8mm spacing c) As the spacing decreased 62% to 4mm εxx strain decreased by 1000% showing a positive, non-linear correlation in the average maximum of the strain d) Mapping max strain magnitudes from the wall to the mid-point showed a convex parabolic strain profile that minimized at the middle**

Difference between experimental and computational lateral strains are affected by
material stiffness as well as friction and damping coefficients

The effect of material stiffness on the average RSME match between DIC
experiments and FE models was quantified using the averaged ε_{xx} distribution at the
positive and negative peaks at 8mm well width for the calibration gels. Using
experimentally measured stiffness and ABAQUS-recommended default values of 0.75
and 0.03 for the friction and damping coefficients, the average match between DIC and
FE at $\pi/2$ timepoint was 0.19 while the average RMSE match between experimental
replicates (between the three wells, Figure 2a) was 0.15, showing that the average
mismatch between FE and DIC was within experimental error. Using default friction and
damping coefficients, increasing or decreasing the measured material stiffness resulted in
average RMSE values of 0.36 and 0.63, respectively which were larger than the
experimental variation and indicated the importance of accurate stiffness measurements
for accurate modeling.

Since the exact boundary conditions between the gels and the PLA was unknown,
we further investigated the possible combinations of friction and damping coefficient
values that could further minimize the average RMSE values. Varying the friction
coefficient between 10 and 0.1 resulted in the average RMSE values of 0.28 and 0.16 at
measured stiffness and default damping coefficient. Similarly, only varying damping
coefficient between values of 0.3 and 0.003 resulted in average RMSE values of 0.28 and
0.3, respectively. Since the gel stiffness was measured experimentally, an empirical linear
DOE model using a 2nd order polynomial was used to find the optimal friction / damping
combination (Table 1). The lowest average RMSE was obtained at the friction / damping

combination of 0.1/0.003 which was 0.16 for the calibration gel which was not further decreased by the DOE model. Shown in Figure 3a, further quantifying the full field RMSE values using a 15x37 grid, the maximum strain difference between the experimental and FE models was largest towards the outer walls. Of this, the largest difference of 0.015 of averaged ε_{xx} magnitude difference occurs in the regions 5 and 6. Regions 3 and 4 are the closest matching, with an averaged ε_{xx} magnitude difference of 0.0047 and 0.0052, respectively. The corner regions (1, 2, 5 and 6) has an averaged ε_{xx} magnitude difference of 0.0077, 0.0079, 0.0113, 0.0122, respectively.

As shown in the supplementary table S1, the lowest averaged RMSE for the HA gel was 0.25. That maximum strain difference was performed identically to the collaboration gel (Figure S4a). The largest difference of 0.024 again occurs in region 6, with regions 3 and 4 (the middle regions) matching the closest with ε_{xx} averages of .0091 and 0.0082, respectively. The corner regions, especially in the actual corners, had average differences of 0.011, 0.010, 0.010, 0.098 for 1, 2, 4, and 5 respectively.

Using the friction / damping coefficient combinations that minimized the average RMSE values between DIC and FE results at 8mm well width, we have quantified the averaged ε_{xx} magnitudes over 6mm, 5mm, and 4mm. The maximum ε_{xx} values were symmetrical at both the $\pi/2$ and t=$3\pi/4$, in addition to both ends of the well, demonstrating steady state. Measuring the averaged ε_{xx} distribution at positive and negative peaks, 20% of the total measured 1300 data point were between 0.03 and 0.026(Supplementary Figure S4b). Minimum strains were also measured halfway between the absolute maxima (t= π). The average maximum values at t= π reached to 0.0041±0.000021, corresponding to 10% of the total number of data points measured at

$t = \pi$ (Supplementary Figure S4c). The $\pi/2$ sets for each spacing over all three trials were again collated into data distribution plots (Figure 3c). We see an even change in extrema differences as the spacing changes. When compared, the surface strain at the 8mm between the averaged maximum ε_{xx} strains of 6mm, 5mm, 4mm, and 3mm well widths decreased to 0.017 ± 0.00040 (-22%, $p<0.05$), 0.013 ± 0.00030 (41%, $p<0.05$), 0.010 ± 0.00037 (-54%, $p<0.05$) , and 0.0026 ± 0.00051 (-88%, $p<0.05$), respectively. Quantifying the strain profiles over the half-width of each well in Figure 3d, showed a somewhat linear relationship between ε_{xx} strains and X- distance, similar to Figure 3c. All distances ε_{xx} strains were statistically different ($p<0.05$).

Table 1   **Design of Experiments**

Stiffness	Friction	Damping	RMSE
1.5	10	0.3	0.41
1.5	10	0.003	0.37
1.5	10	0.03	0.47
1.5	0.1	0.3	0.50
1.5	0.1	0.003	0.38
1.5	0.1	0.03	0.38
1.5	0.75	0.3	0.35
1.5	0.75	0.003	0.36
1.5	0.75	0.03	0.36
0.5	10	0.3	0.53
0.5	10	0.003	0.45
0.5	10	0.03	0.56
0.5	0.1	0.3	0.58
0.5	0.1	0.003	0.50
0.5	0.1	0.03	0.49
0.5	0.75	0.3	0.63
0.5	0.75	0.003	0.64
0.5	0.75	0.03	0.63
1	10	0.3	0.29
1	10	0.003	0.28
1	10	0.03	0.28
1	0.1	0.3	0.16
1	0.1	0.003	0.16
1	0.1	0.03	0.16
1	0.75	0.3	0.30
1	0.75	0.003	0.28
1	0.75	0.03	0.19

The FE model mirrors the experimental positive correlation between distance and maximum strain but predicts higher strains at the wall surfaces. Unlike the experimental DIC data, the negative strain was found to be on average, 22% larger than the positive strain (Figure 3c). With for the 8mm curve, we see a similar parabolic convex curve from the wall to the midpoint, however the strain magnitude is larger (Figure 3d). ε_{xx} strain magnitude over the cycle varied similarly to the DIC experimental data, however the values were around double those of the DIC experiments(Figures 2d and 3d). The percent

differences between experimental and FE 8-4mm spacings at the wall were, respectively,

155%, 110%, 75%, 233%, and 3250. The FE model was 144% larger than the

experimental DIC.
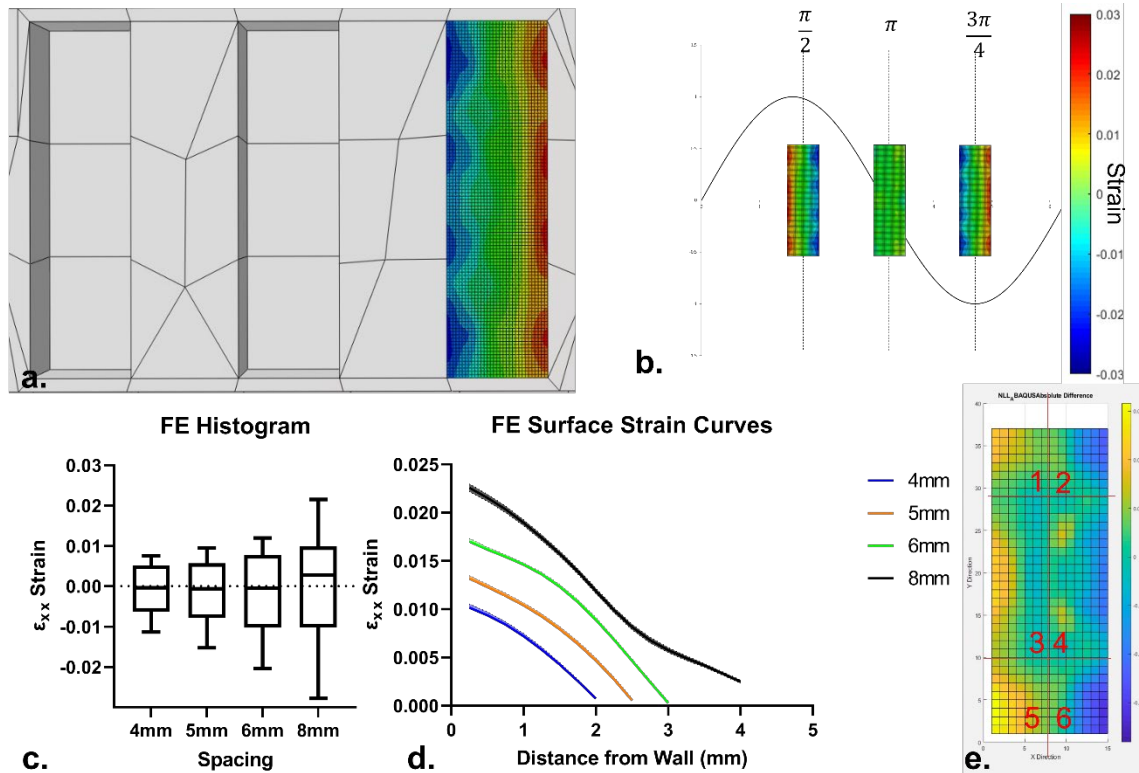
Figure 3   a) Finite Element (FE) model experimental setup. Model is the 8mm spacing. Wells were vibrated identically to the experimental data. Each FE run was proceeded by a gravity step on the gel b) εxx strain magnitude over the cycle. The strain magnitudes were around 2x those of the experimental DIC c) Shows a linear relationship between the maximum magnitude and the wall spacing. Generally, the negative strain is larger than the positive d) Mapping the maximum strain magnitudes, we see a similar convex parabolic curve with each spacing, excluding 8mm e) The difference between the surface of DIC experimental and the FE model. Most of the difference occurs on the outside, especially the outer edge. We also see about twice the maximum magnitude.

Finite element modeling shows a significant difference between the strain in 13.5% and
25% bone volume

All bone marrow data over the final cycle was extracted and combined into a
single histogram. The resulting data was divided into $\sqrt{N}$ bins where N is the total
number of points in the 13.5% BV/TV, resulting in 3588 evenly spaced bins. There is a
large difference between the apparent maximum values, and a large concentration of the
total points in the center (towards zero) of each of the tensors (Figures 4c and 4d)

The FE simulations show there is a difference between nearly all components of
strain between the 13.5% and 25% BV fill scaffolds. For the 13.5% the normal ε_{xx}, ε_{yy}
and ε_{zz} strains had extrema of -0.053/ 0.062, -0.056/ 0.071, and -0.075/ 0.067
respectively, with ε_{xy}, ε_{yz} and ε_{zx} strain extrema of -0.102/ 0.067, -0.082/ 0.104. The 25%
BV/TV had ε_{xx}, ε_{yy} and ε_{zz} extrema of -0.047/ 0.012, -0.017/ 0.050, and -0.047/0.029.
The shear ε_{xy}, ε_{yz} and ε_{zx} strain had extrema of -0.023/ 0.025, -0.042/ 0.053, and -0.021/
0.062 (table 2). There was a significant difference (P< 0.05) between the von mises strain
of the 13.5% and 25%, and additionally the ε_{zz}, ε_{xy} and ε_{yz} strains, but not (P > 0.05) the
ε_{xx}, ε_{yy}, and ε_{zx} strains in the two samples. Overall, the 13.5% had higher strain
magnitudes in all components, including Von Mises Strain. following the results of the
DIC experimental data of a positive relationship between the strain distance and the strain
magnitude.

To greater understand the histograms, we examined the strain distributions over
the 3D models. Both sizes showed an incredibly large amount of volume at or near zero
strain (shown in green), which would account for the large cluster in the histograms
(Figure 4e and 4f). We also see that the largest distributions are at or near the contact

points, with Figure 4e showing large stresses between the scaffold contact points, and almost zero everywhere else. Even when cut along the x and z axis (Figures 4g-4j) we see that the stresses are exclusively around the contact between the scaffold and the gel, as we might expect, but that these strains do not radiate very far beyond these contact points. Each of these Figures, especially the difference between Figures 4i and 4j, demonstrate that the maximum values shown in the 13.5% are much larger than the values in the 25%, validating that the spacing does indeed increase the overall strain.
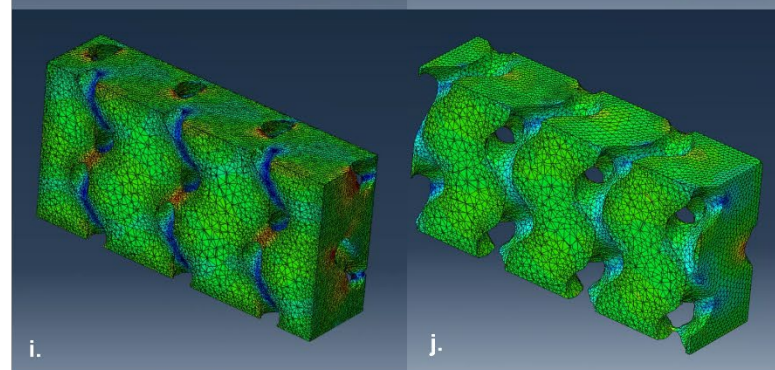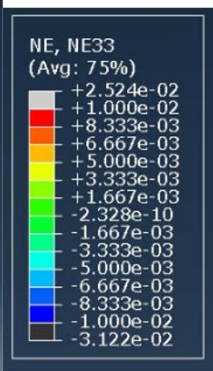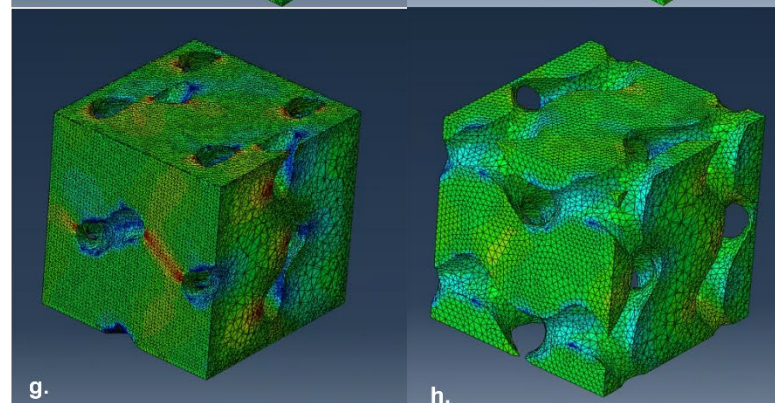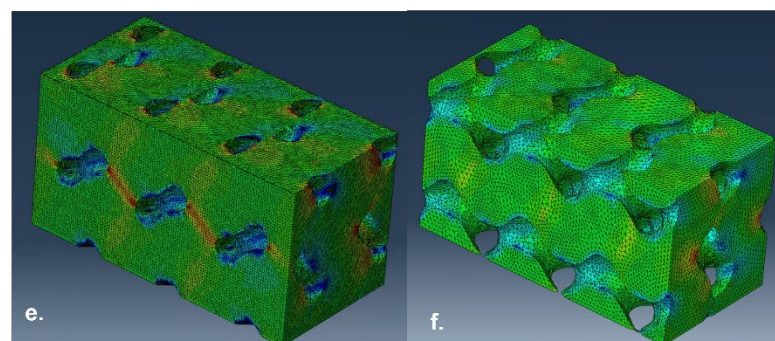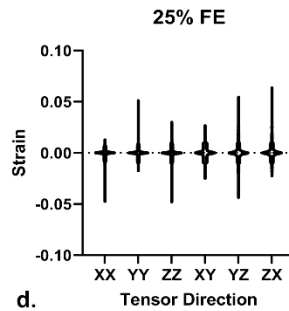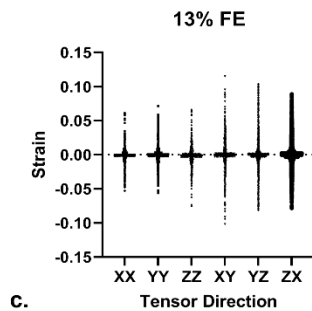
13% FE   25% FE
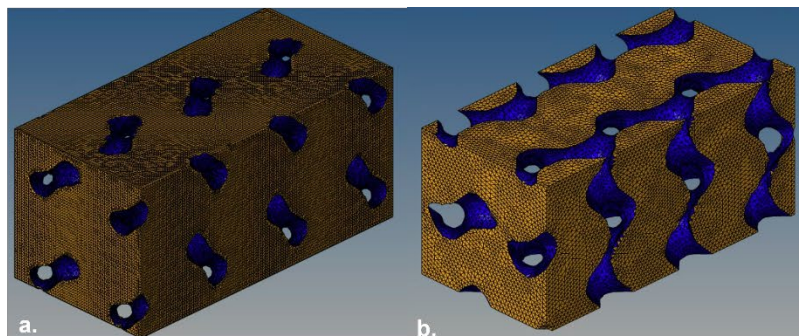
Figure 4   **a) 13% Scaffold hypermesh, where the yellow corresponds to the deformable marrow elements, and the blue the rigid bone elements. Mesh was created using 14mm cell size, and tetragonal or triangular elements b) 25% scaffold, with yellow tetragonal elements corresponding to the deformable marrow and blue triangular elements corresponding to rigid bone elements. Both the 13% and 25% geometries were generated as gyroid c) the strain distribution over a single cycle, for each of the 6 strain tensors in the 13.5% scaffold d) the strain distribution over a single cycle, for each of the 6 strain tensors in the 25% scaffold e) 13.5% element at its maximum strain values (similar to Figures 2 and 3) for the Z direction strain tensor f) 25% element at its maximum strain values (similar to Figures 2 and 3) for the Z direction strain tensor g) Figure e cut along the x plane, showing the internal elements internal strain values h) Figure f also cut along the x plane, showing much lower overall strain values compared to the 13.5% i) Figure e cut along the z axis, allowing us to view the high stress concentrates primarily along the interaction points with the bone scaffold j) Figure f cut along the z axis, showing a similar but much smaller response to that in Figure i.**

Table 2   **HA Design of Experiments**

Tensor	13.5%		25%	
	Min	Max	Min	Max
XX	-0.053	0.062	-0.047	0.012
YY	-0.056	0.071	-0.017	0.050
ZZ	-0.075	0.067	-0.047	0.029
XY	-0.102	0.067	-0.023	0.025
YZ	-0.082	0.104	-0.042	0.053
ZX	-0.078	0.089	-0.021	0.062

<u>Genes of interest show a correlation with percent bone volume and vibrated vs non-vibrated</u>

Collagen-I immunostaining demonstrates a denser collagen structure in vibrated samples, vs non vibrated, though at roughly the same apparent distribution (Figure 5a-b). PCR performed on HA cellular RNA demonstrates positive a trend between the expression of Col-I between LIV – and LIV + samples (Figure 5c). Immunostaining analysis agreed with the PCR trend, collagen-I immunostaining demonstrated a positive relationship between LIV – and LIV +, but also a correlation with BV/TV, with significant differences between both variables (Figure 5d). e-g) Ki-67 proliferation

expression at 0%, 25% LIV – and 25% LIV + sees an increase in the stained cell size with LIV – and LIV +, with little apparent difference between the two LIV – samples (Figures e-g). Quantitate analysis of immunostaining reached a statistically significant difference in the Ki-67 proliferation expression only in the 25% scaffold exclusively, with no significance between the LIV – and LIV + 13.5% scaffolds (Figure 5h). One of the most noticeable effects of LIV can be seen in the increase in F-Actin (filamentous actin). F-Actin staining (green) showed a larger expression in vibrated samples, predominantly on cells adhered to the surface of PLA (Figure 5i). F-actin heavy cell structures were found largely on the surface on the PLA bone structure. (Figure 5j). To ensure cell viability, live dead stains were performed at the end of the 14 day vibration trial which showed a large number of live cells, and few dead cells (Figure 5k).
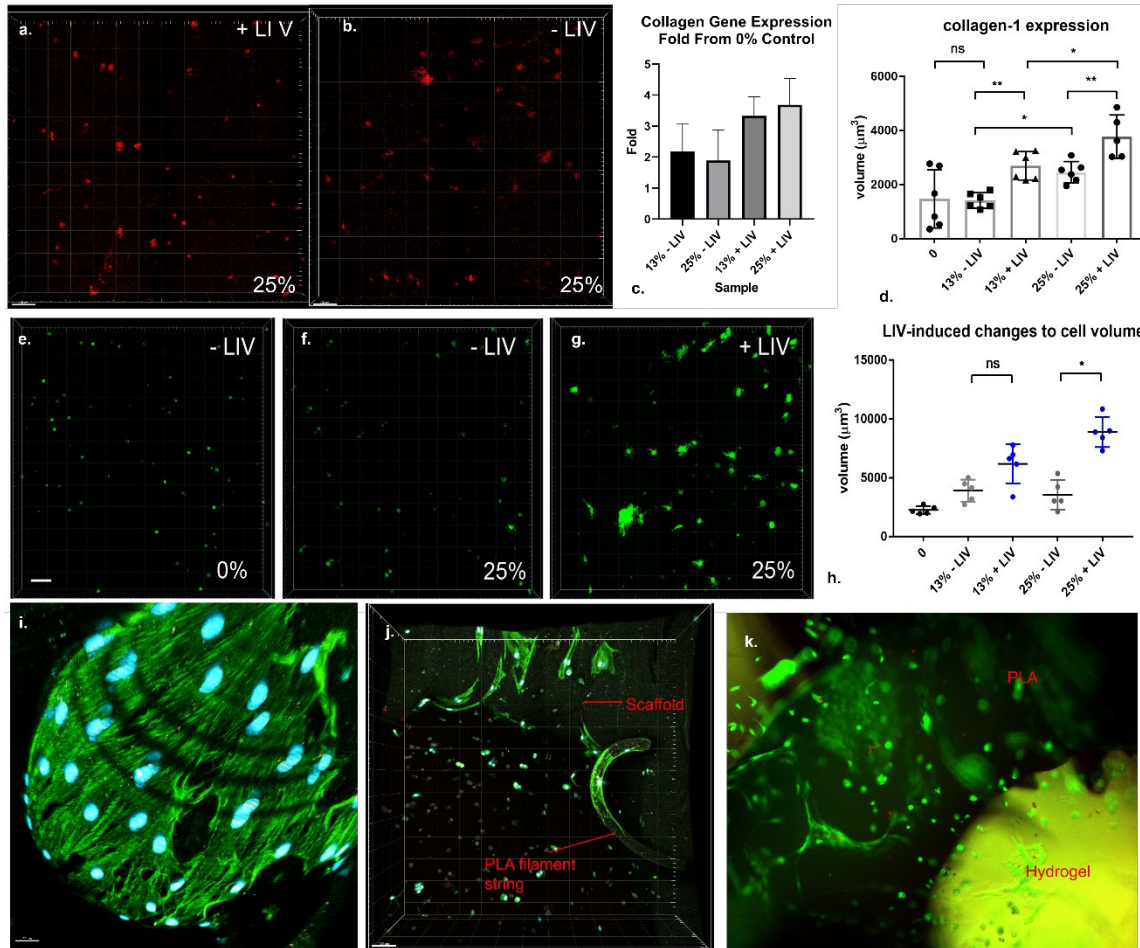
Figure 5 **a-b) Red stained collagen 1 in the vibrated and un-vibrated 25% scaffolds, respectively c) PCR results showing a trend in the fold difference from the 0% scaffold-less gels in Collagen – I gene expression. We see a trend between LIV and an increase in the corresponding scaffolds' expression of Collagen – I d) Immunostaining results show a significant increase in both LIV + and -, but also between 13% and 25% scaffolds e-g) Ki-67 expression at 0%, 25% and 25% and LIV -, - and +. We see an increase in the stained cell size with LIV h) quantitate results reach a statistically significant difference only in the Ki-67 proliferation expression only in the 25% scaffold i) F-Actin staining (green) and nuclear envelope staining (blue) of MSCs on the surface of a 3D printed, 25% BV vibrated scaffold j) 25% bone volume fill with adhered MSCs on a PLA filament remnant from printing k) live dead imaging with red being dead cells and green being live cells. Performed at the end of a 14-day vibration to ensure cell viability long term**

4. Discussion

We have shown that the strain between a representative young and aged individual have statistically significant strain responses. Previous studies with fluid shear tend to rely on the viscosity and fluid description of their model material without any biological validation[56], however ours offers an experimentally validated model which describes cellular response in a physiologically similar model.

There is a statistically significant different response to the BV (bone volume)/ TV (trabecular volume/total volume) of 25% and 13.5% within the finite element model. While some portions of the model' strains demonstrate no significance (P<0.05), the overall von mises strain shows a significance (P< 0.05), between the two geometries' strain. We have a parallel strain (parallel to the direction of vibration) which is statistically different between the 13.5% and 25% (aged and young bone). Aligning with previous experiments in DIC, the 13.5% (possessing a smaller trabecular volume, thus a larger spacing) has an overall statistically significant von mises, and ε_{zz} (the direction of vibration in the FE model), strain between the two models. The 3D FE models show a statistically significant overall strain difference, however the ε_{xx}, ε_{yy}, and ε_{zx} do not show a significant difference.

Unlike our vibrated 2D model, where we compared only the x direction strain tensor, there is no single tensor which we can quantify. Instead, all modes of normal and shear strain show significant values over the entire cycle. This also means that different maximum values occur at different moments in the excitation cycle. For instance, the maximum z strain, which was shown in Figure 5, reaches a maximum in phase with the excitation, but y and x are about a quarter out of phase of the excitation. Thus, the total

strain at any given timepoint is likely much larger than zero, however its components are in other tensors.

While we do see a difference between the two scaffolds, the strain is largely contained within the immediate vicinity of the scaffold. Additionally, we would expect that the larger strains experienced in the 13.5% would correlate to higher cell activity, but our cell data does not agree. Instead we see an increase in all measured activity. The FE model contains an inherent bias; all our previous data from surface modelling predicts that the larger spacing distance (13.5%) will exhibit a larger FE strain, which our model corroborates. While this seems to contradict pre-established data, the timeframe of this study introduces avenues of further constraint and study. While it is true that we would expect a larger strain to demonstrate an increase in collagenous genes[85], we also only demonstrate a 2-week biological window to extrapolate data. An alternate interpretation of the increase in collagen, Ki-67 and F-Actin expression in this window is a lack of structure within the 13.5% scaffold to justify this response to LIV.

Additionally, our methods of measuring the cell response may factor into the increase we demonstrate. When imaging, the 25% scaffold has much smaller amounts of gel relative to the scaffold, so for any given cell we image, it is more likely to be closer to the wall. From our FE data, this would put that cell in a larger region of strain, thus demonstrate a response to higher strain. This same behavior could also explain the larger responses we see in biological models (Figures 5c, 5d, 5h). If a cell is more likely to be closer to the scaffold wall, then it will exhibit a response to strain.

The measured PCR results demonstrate a trend towards more collagen-I expression in the vibrated samples, over the control samples. This increase has been

documented in multiple other studies as a response to vibration[85]. Most of the RNA extracted from the samples was from cells within the gel, and while the cells remaining on the scaffold were examined, there was not enough RNA to successfully analyze with PCR.

There is a small difference between our DIC experimental data and our FE model, in both our calibration and HA gels. To be clear, the average RMSE values between individual wells in in a single calibration experiment (example: three wells in Figure 2a) is 0.148, almost identical to the calibration gels value of 0.156. While the HA exhibits an RMSE 0.25, still very close to the average RMSE within a single experiment. We have two potential explanations for this. The first has to do with the assumption of our PLA model is a rigid body. While this appears to be a valid assumption[82], early experimentation with 1mm thick walls demonstrated vibrational interference would occur through the walls of each well. There is a potential weakness in the model not accounting for strain damping that the walls potentially provide, which would decrease the wall strain stiffness in the FE model.

The second explanation emanates from limitations in the methods of DIC itself. Generally, DIC is less accurate towards the outer edges of a samples, and the best practices recommends the exclusion of the outer 10% of a sample's boundary.[15,16] However, as MSCs tend to be at or near the boundary of trabecular bone, we felt capturing the effects near the boundary are important for verifying the accuracy of the model. This limitation of DIC techniques could be under-estimating the magnitudes towards the walls of the model. This explanation can be reinforced with the discussion of the 3mm wall thickness. At this wall thickness (and lower, as 2mm was taken), DIC has

untrustworthy effects, where the 3mm and 2mm are limited by hardware resolution limitations, restricting the viable strain profiles, reducing the smaller spacings to mere noise.

Next are the analysis of the pure FE model. First, while the two models share an identical marrow density, this creates an inherent flaw between the two models: the different number of data points. Inherently, we expect about 1.85x the amount of data points in the overall 13.5v 25 BV/TV structures, which is the roughly amount we are presented with (6.1 vs 12.8 million data points (2.09)). Not only would we expect larger magnitudes of nodes at identical densities, but we would expect a larger strain value, from the DIC experimental data. This holds true in the FE data; the 13.5% aged bone shows a larger strain magnitude than the young 25% bone. This doesn't fully account for the difference in cellular data that we would expect (as will be discussed later), since the younger (and hence stiffer) marrow does not correlate with a larger expected strain magnitude, instead the older bone is expected to produce a larger strain magnitude.

CHAPTER FOUR: CONCLUSIONS

4.1 Summary

We have developed a novel 3D scaffold with a validated finite element model in order to explore the relationship between bone mechanical environment and cellular response. We used this model to compare two scaffold sizes, 13.5% and 25% corresponding to aged and healthy bone, respectively. We were able to correlate the spacing to the resulting strain environment and cellular response via immunostaining and PCR, and reject the null hypothesis, showing there is a correlation between the spacing and the mechanical response.

4.2 Limitations

While we were able to create a validated model, there are limitations in its application. Limitations included, but were not limited to: assumptions, human error, budgetary concerns, specific geometries and processing power. At its core, the limitations of our model involve our selection of a marrow replacement. As has been previously found, one of the primary methods to characterize marrow is as a viscous fluid. While it still exhibits elastic behavior, the predominant response is viscous[38,39,56]. Our model using Hyaluronic acid presents the opposite case, being a predominantly elastic behavior, which still exhibits viscous behavior.

However, when it comes to direct comparisons of values, ours are close to previously measured ranges (Moduli of 0.25-24.7kPa and a viscosity of 37.5-1000 cP)[36,37] although any characterization of bone marrow should be taken with a healthy

skepticism. This comes in part from the extreme difficulty and variability of testing the mechanical properties of bone marrow. Storage and even measurement technique can affect the results. For example, it has been reported that an order of magnitude larger viscosity when measuring fresh versus frozen marrow, likely from the disruption ice crystals had on the stability of the ECM[22]. With the exception of one, all cited papers which report a rheological value, removed bone marrow via syringe (which would destroy any extracellular matrix, ECM) and then tested, and rheological measurements would ensure that any remaining ECM was non-viable. Despite this, there remains any form of measurement which does not rely on some sort of invasive, destructive method to measure the properties of marrow. Even if there were some ideal method of measurement it is unlikely that would make any difference, as the heterogenous nature of marrow would limit this measurement to only that specific sample tested. Thus, FE modeling of ideal structures remains an necessary tool to understanding marrow mechanical environment.

The assumption of a rigid body is a significant limitation in our study. As previously discussed, we believe that the differences exhibited in the DIC vs finite element modeling has many potential answers, but one is the assumption of the tray as a rigid body. Early experiments conducted had thin walled fins, and many more wells. We observed interference between these structures, which lead to the current interation of the tray design (Supplementary Figure 5 vs Figure 2a). The necessity of modeling the structure as a rigid body would also lead to an increase in computation time, which we will discuss further below

Our FE model has only been validated under a very specific set of circumstances to match our physical model. This limits its applicability under different frequencies, accelerations, and temperatures which are known to change the mechanical properties exhibited by hydrogels and other viscoelastic materials. Furthermore, as we are using an MMP cleavable hydrogel, it is expected that the cells would be modifying their environment over the 14 day vibration period, however the extent of this modification is unknown, limiting the material characterization if there is a large change in properties. This assumption simplifies the modeling process, but also potentially puts a lifetime on the accuracy of the model.

Our model also has limitations in resolution. Due to the complex geometry we are attempting to model, a large computational time is required for even a single, 5 cycle simulation, we experienced simulation times of 4-8 days. To increase the accuracy, the obvious solution would be to increase the complexity of elements, but this leads to exponentially increasing computation time required to analyze a given set of data. Increasing that time further limits the analytical potential of our model in other research.

Finally, our model demonstrates that the largest amount of strain is at or near the contact points between the scaffold and the gel. This makes it vital to image the cells in both scaffolds at the same distance from the wall. This may or may not have been achieved, and further work is required as the demonstrated cell behavior could be a ghost from our measurement techniques, as explored in the discussion of the manuscript, the smaller spacing in the 25% makes it much more likely we will image a cell which is close to a wall than the 13.5%, and further study is needed to explore whether the demonstrated cell response is real.

Budget was also a concern for the project. Hyaluronic acid is prohibitively expensive, and while with the calibration gel we performed 12 sets of material characterization and 3 trials of DIC validation, we were only able to perform 3 sets of characterization and 1 trial (with only a single successfully cross-linked well) the accuracy of the data we are matching the FE model to is suspect.

4.3 Future Work

This work has served as the foundation for a continued experiment in which these same scaffolds and model will be sent to the ISS to study the effects of vibration in microgravity, but this model could be improved so that these and future projects can more confidently draw conclusions from future analysis.

The first is to fully characterize the scaffold-hydrogel interactions, and accurately model the PLA scaffold. This allows future studies using different types of material, perhaps even more biochemically accurate materials such as hydroxyapatite. A more rigorous characterization of Hyaluronic acid would also benefit the accuracy of the model, as this study's resources were limited in producing more data trials.

Next, an exploration of how MSCs change the marrow mechanical environment. Testing the mechanical properties of the HA as it is vibrated would not only offer insight into how the MSCs are modifying their environment, but also give a more accurate characterization to the model. Sampling of media for concentrations of hyaluronidase and other proteins that would measure the modification rate in conjunction with mechanical testing throughout the experiment could improve the model, or clearly define the timeframe the model is relevant.

Finally, a more rigorous exploration of the seeming conflict between the measured larger strain in the 13.5% scaffold, but a lower cell response needs to be conducted. Whether this is a result of smaller strain requiring more intricate cell networks, or from imaging techniques. If it isn't the result of imaging, then this could show that there is something else about the 25% scaffold causing a difference in cell response. Perhaps it is the curvature, pure acceleration or interactions in the bone marrow which we did not account for in our model.

Further manipulation of the replicant bone marrow enables more rigorous studies to be conducted.

REFERENCES

1   Steward, A. J. & Kelly, D. J. Mechanical regulation of mesenchymal stem cell differentiation. **227**, doi:10.1111/joa.12243 (2015).

2   Ullah, I., Subbarao, Raghavendra B. & Rho, Gyu J. Human mesenchymal stem cells - current trends and future prospective. **35**, doi:10.1042/BSR20150025 (2015).

3   Rohban, R. & Pieber, T. R. Mesenchymal Stem and Progenitor Cells in Regeneration: Tissue Specificity and Regenerative Potential. **2017**, doi:10.1155/2017/5173732 (2017).

4   Hao, J. *et al.* Mechanobiology of mesenchymal stem cells: Perspective into mechanical induction of MSC fate. **20**, doi:10.1016/j.actbio.2015.04.008 (2015).

5   Rubin, C. T. & Lanyon, L. E. Regulation of bone mass by mechanical strain magnitude. *Calcified tissue international* **37**, 411-417 (1985).

6   Rubin, C. T. & Lanyon, L. E. Regulation of bone formation by applied dynamic loads. *The Journal of bone and joint surgery. American volume* **66**, 397-402 (1984).

7   O'Connor, J. A., Lanyon, L. E. & MacFie, H. The influence of strain rate on adaptive bone remodelling. *J Biomech* **15**, 767-781 (1982).

8   Rath, B., Nam, J., Knobloch, T. J., Lannutti, J. J. & Agarwal, S. Compressive forces induce osteogenic gene expression in calvarial osteoblasts. *Journal of Biomechanics* **41**, 1095-1103, doi:10.1016/j.jbiomech.2007.11.024 (2008).

9   Poliachik, S. L., Threet, D., Srinivasan, S. & Gross, T. S. 32 wk old C3H/HeJ mice actively respond to mechanical loading. *Bone* **42**, 653-659, doi:10.1016/j.bone.2007.12.222 (2008).

10   McGarry, J. G., Klein-Nulend, J., Mullender, M. G. & Prendergast, P. J. A comparison of strain and fluid shear stress in stimulating bone cell responses--a computational and experimental study. *FASEB J* **19**, 482-484, doi:10.1096/fj.04-2210fje (2005).

11   Sikavitsas, V. I., Bancroft, G. N., Holtorf, H. L., Jansen, J. A. & Mikos, A. G. Mineralized matrix deposition by marrow stromal osteoblasts in 3D perfusion culture increases with increasing fluid shear forces. *Proc Natl Acad Sci U S A* **100**, 14683-14688, doi:10.1073/pnas.2434367100 (2003).

12   Bancroft, G. N. *et al.* Fluid flow increases mineralized matrix deposition in 3D perfusion culture of marrow stromal osteoblasts in a dose-dependent manner. *Proc Natl Acad Sci U S A* **99**, 12600-12605, doi:10.1073/pnas.202296599 (2002).

13   Weinbaum, S., Cowin, S. C. & Zeng, Y. A model for the excitation of osteocytes by mechanical loading-induced bone fluid shear stresses. *J Biomech* **27**, 339-360 (1994).

14   Reich, K. M., Gay, C. V. & Frangos, J. A. Fluid shear stress as a mediator of osteoblast cyclic adenosine monophosphate production. *J Cell Physiol* **143**, 100-104, doi:10.1002/jcp.1041430113 (1990).

15   Rubin, C., Turner, A. S., Bain, S., Mallinckrodt, C. & McLeod, K. Anabolism. Low mechanical signals strengthen long bones. *Nature* **412**, 603-604, doi:10.1038/35088122 (2001).

16   Oxlund, B. S., Ortoft, G., Andreassen, T. T. & Oxlund, H. Low-intensity, high-frequency vibration appears to prevent the decrease in strength of the femur and tibia associated with ovariectomy of adult rats. *Bone* **32**, 69-77, doi:10.1016/s8756-3282(02)00916-x (2003).

17   Tanaka, S. M. *et al.* Effects of broad frequency vibration on cultured osteoblasts. *J Biomech* **36**, 73-80 (2003).

18   Garman, R., Gaudette, G., Donahue, L. R., Rubin, C. & Judex, S. Low-level accelerations applied in the absence of weight bearing can enhance trabecular

bone formation. *Journal of orthopaedic research : official publication of the Orthopaedic Research Society* **25**, 732-740, doi:10.1002/jor.20354 (2007a).

19   Wren, T. A. *et al.* Effect of high-frequency, low-magnitude vibration on bone and muscle in children with cerebral palsy. *J Pediatr Orthop* **30**, 732-738, doi:10.1097/BPO.0b013e3181efbabc (2010).

20   Pre, D. *et al.* The differentiation of human adipose-derived stem cells (hASCs) into osteoblasts is promoted by low amplitude, high frequency vibration treatment. *Bone* **49**, 295-303, doi:10.1016/j.bone.2011.04.013 (2011).

21   Coughlin, T. R. & Niebur, G. L. Fluid shear stress in trabecular bone marrow due to low-magnitude high-frequency vibration. *Journal of Biomechanics* **45**, 2222-2229, doi:10.1016/j.jbiomech.2012.06.020 (2012).

22   Metzger, T. A., Shudick, J. M., Seekell, R., Zhu, Y. & Niebur, G. L. Rheological behavior of fresh bone marrow and the effects of storage.   **40**, doi:10.1016/j.jmbbm.2014.09.008 (2014).

23   Raic, A., Naolou, T., Mohra, A., Chatterjee, C. & Lee-Thedieck, C. 3D models of the bone marrow in health and disease: yesterday, today, and tomorrow.   **9**, doi:10.1557/mrc.2018.203 (2019).

24   Uzer, G. *et al.* Cell Mechanosensitivity to Extremely Low-Magnitude Signals Is Enabled by a LINCed Nucleus. *STEM CELLS* **33**, 2063-2076, doi:10.1002/stem.2004 (2015).

25   Vogel, V. & Sheetz, M. Local force and geometry sensing regulate cell functions. **7**, doi:10.1038/nrm1890 (2006).

26   Uzer, G. *et al.* Cell Mechanosensitivity to Extremely Low-Magnitude Signals Is Enabled by a LINCed Nucleus.   **33**, doi:10.1002/stem.2004 (2015).

27   Li, L., Dong, L., Wang, Y., Zhang, X. & Yan, J. <i>Lats1/2</i> -Mediated Alteration of Hippo Signaling Pathway Regulates the Fate of Bone Marrow-Derived Mesenchymal Stem Cells.   **2018**, doi:10.1155/2018/4387932 (2018).

28   Driscoll, Tristan P., Cosgrove, Brian D., Heo, S.-J., Shurden, Zach E. & Mauck, Robert L. Cytoskeletal to Nuclear Strain Transfer Regulates YAP Signaling in Mesenchymal Stem Cells. **108**, doi:10.1016/j.bpj.2015.05.010 (2015).

29   Fulford, A. D. & McNeill, H. Fat/Dachsous family cadherins in cell and tissue organisation. **62**, doi:10.1016/j.ceb.2019.10.006 (2020).

30   Crespo-Enriquez, I. *et al.* Dchs1-Fat4 regulation of osteogenic differentiation in mouse. **146**, doi:10.1242/dev.176776 (2019).

31   Thompson, M. *et al.* Low-intensity vibration restores nuclear YAP levels and acute YAP nuclear shuttling in mesenchymal stem cells subjected to simulated microgravity. **6**, doi:10.1038/s41526-020-00125-5 (2020).

32   Mehta, S. *et al.* The effect of low-magnitude, high-frequency vibration on poly(ethylene glycol)-microencapsulated mesenchymal stem cells. **9**, doi:10.1177/2041731418800101 (2018).

33   Titorencu, I., Pruna, V., Jinga, V. V. & Simionescu, M. Osteoblast ontogeny and implications for bone pathology: an overview. **355**, doi:10.1007/s00441-013-1750-3 (2014).

34   Hanna, H., Mir, L. M. & Andre, F. M. In vitro osteoblastic differentiation of mesenchymal stem cells generates cell layers with distinct properties. **9**, doi:10.1186/s13287-018-0942-x (2018).

35   Turner, C. H., Owan, I. & Takano, Y. Mechanotransduction in bone: role of strain rate. **269**, doi:10.1152/ajpendo.1995.269.3.E438 (1995).

36   Jansen, L. E., Birch, N. P., Schiffman, J. D., Crosby, A. J. & Peyton, S. R. Mechanics of intact bone marrow. **50**, doi:10.1016/j.jmbbm.2015.06.023 (2015).

37   Gurkan, U. A. & Akkus, O. The Mechanical Environment of Bone Marrow: A Review. **36**, doi:10.1007/s10439-008-9577-x (2008).

38   Curtis, K. J., Oberman, A. G. & Niebur, G. L. Effects of mechanobiological signaling in bone marrow on skeletal health. **1460**, doi:10.1111/nyas.14232 (2020).

59

39 Coughlin, T. R., , Niebur, G. L. & Fluid shear stress in trabecular bone marrow due to low-magnitude high-frequency vibration. **45**, doi:10.1016/j.jbiomech.2012.06.020 (2012).

40 Fung, Y. C. Biomechanics: Mechanical properties of living tissues. (1981).

41 Yang, Y. B. & Hung, H. H. A 2.5D finite/infinite element approach for modelling visco-elastic bodies subjected to moving loads. **51**, doi:10.1002/nme.208 (2001).

42 Lee, T., Lakes, R. S. & Lal, A. Resonant ultrasound spectroscopy for measurement of mechanical damping: Comparison with broadband viscoelastic spectroscopy. **71**, doi:10.1063/1.1150703 (2000).

43 Tack, P., Victor, J., Gemmel, P. & Annemans, L. 3D-printing techniques in a medical setting: a systematic literature review. **15**, doi:10.1186/s12938-016-0236-4 (2016).

44 Schubert, C., van Langeveld, M. C. & Donoso, L. A. Innovations in 3D printing: a 3D overview from optics to organs. **98**, doi:10.1136/bjophthalmol-2013-304446 (2014).

45 Haq, J., Patel, N., Weimer, K. & Matthews, N. S. Single stage treatment of ankylosis of the temporomandibular joint using patient-specific total joint replacement and virtual surgical planning. **52**, doi:10.1016/j.bjoms.2014.01.004 (2014).

46 Lee, J., Yeo, M., Kim, W., Koo, Y. & Kim, G. H. Development of a tannic acid cross-linking process for obtaining 3D porous cell-laden collagen structure. **110**, doi:10.1016/j.ijbiomac.2017.10.105 (2018).

47 Wu, Q., Zhang, X., Wu, B. & Huang, W. Effects of microwave sintering on the properties of porous hydroxyapatite scaffolds. **39**, doi:10.1016/j.ceramint.2012.08.091 (2013).

48 Wang, H. *et al.* Osteogenic effect of controlled released rhBMP-2 in 3D printed porous hydroxyapatite scaffold. **141**, doi:10.1016/j.colsurfb.2016.02.007 (2016).

49   Inzana, J. A. *et al.* 3D printing of composite calcium phosphate and collagen scaffolds for bone regeneration. **35**, doi:10.1016/j.biomaterials.2014.01.064 (2014).

50   Su, X., Wang, T. & Guo, S. Applications of 3D printed bone tissue engineering scaffolds in the stem cell field. **16**, doi:10.1016/j.reth.2021.01.007 (2021).

51   Keating, T. J., Wolf, P. R. & Scarpace, F. L. An improved method of digital image correlation. **41**, 993-1002 (1975).

52   Read, D., Cheng, Y.-W. & Sutton, M. Proposed Standardization Effort: Digital-Image Correlation for Mechanical Testing. (1970).

53   Nesbitt, D. Q., Siegel, D. N., Nelson, S. J. & Lujan, T. J. Effect of age on the failure properties of human meniscus: High-speed strain mapping of tissue tears. **115**, doi:10.1016/j.jbiomech.2020.110126 (2021).

54   Plevris, V. & Markeset, G. Educational Challenges in Computer-based Finite Element Analysis and Design of Structures. **14**, doi:10.3844/jcssp.2018.1351.1362 (2018).

55   Hirabayashi, S. & Iwamoto, M. Finite element analysis of biological soft tissue surrounded by a deformable membrane that controls transmembrane flow. **15**, doi:10.1186/s12976-018-0094-9 (2018).

56   Dickerson, D. A. *et al.* Modeling the mechanical consequences of vibratory loading in the vertebral body: microscale effects. **7**, doi:10.1007/s10237-007-0085-y (2008).

57   Dickerson, D. A., Sander, E. A. & Nauman, E. A. Modeling the mechanical consequences of vibratory loading in the vertebral body: microscale effects. *Biomech. Model. Mechanobiol.* **7**, 191-202, doi:10.1007/s10237-007-0085-y (2008).

58   Li, D. *et al.* Optimal design and modeling of gyroid-based functionally graded cellular structures for additive manufacturing. **104**, doi:10.1016/j.cad.2018.06.003 (2018).

59   Zhu, J. *et al.* Finite element analysis of trabecular bone with bone marrow fat. doi:10.1109/TENCON.2013.6718957 (2013).

60   Qin, Y. X. & Hu, M. Intramedullary pressure induced by dynamic hydraulic pressure stimulation and its potential in treatment of osteopenia. *Bone* **48**, S186-S186, doi:10.1016/j.bone.2011.03.432 (2011).

61   Qin, Y. X. & Lam, H. Y. Intramedullary pressure and matrix strain induced by oscillatory skeletal muscle stimulation and its potential in adaptation. *Journal of Biomechanics* **42**, 140-145, doi:10.1016/j.jbiomech.2008.10.018 (2009).

62   Zhang, P., Su, M., Liu, Y. L., Hsu, A. & Yokota, H. Knee loading dynamically alters intramedullary pressure in mouse femora. *Bone* **40**, 538-543, doi:10.1016/j.bone.2006.09.018 (2007).

63   Chan, M. E., Uzer, G. & Rubin, C. T. The Potential Benefits and Inherent Risks of Vibration as a Non-Drug Therapy for the Prevention and Treatment of Osteoporosis. *Curr Osteoporos Rep* **11**, 36-44, doi:10.1007/s11914-012-0132-1 (2013).

64   Price, C., Zhou, X., Li, W. & Wang, L. Real-time measurement of solute transport within the lacunar-canalicular system of mechanically loaded bone: direct evidence for load-induced fluid flow. *J Bone Miner Res* **26**, 277-285, doi:10.1002/jbmr.211 (2011).

65   Vainionpaa, A. *et al.* Intensity of exercise is associated with bone density change in premenopausal women. *Osteoporosis Int* **17**, 455-463, doi:10.1007/s00198-005-0005-x (2006).

66   Fritton, S. P., McLeod, K. J. & Rubin, C. T. Quantifying the strain history of bone: spatial uniformity and self-similarity of low-magnitude strains. *Journal of Biomechanics* **33**, 317-325, doi:10.1016/s0021-9290(99)00210-9 (2000).

67   Pagnotti, G. M. *et al.* Combating osteoporosis and obesity with exercise: leveraging cell mechanosensitivity. *Nature Reviews Endocrinology*, doi:10.1038/s41574-019-0170-1 (2019).

68   Marin-Cascales, E. *et al.* Whole-body vibration training and bone health in postmenopausal women: A systematic review and meta-analysis. *Medicine* **97**, e11918, doi:10.1097/md.0000000000011918 (2018).

69   Gilsanz, V. *et al.* Low-Level, High-Frequency Mechanical Signals Enhance Musculoskeletal Development of Young Women With Low BMD. *J.Bone Miner.Res.* **21**, 1464-1474 (2006).

70   Ritzmann, R., Stark, C. & Krause, A. Vibration therapy in patients with cerebral palsy: a systematic review. *Neuropsychiatric disease and treatment* **14**, 1607-1625, doi:10.2147/ndt.s152543 (2018).

71   Mogil, R. J. *et al.* Effect of Low-Magnitude, High-Frequency Mechanical Stimulation on BMD Among Young Childhood Cancer Survivors: A Randomized Clinical Trial. *JAMA Oncol*, doi:10.1001/jamaoncol.2015.6557 (2016).

72   Rubin, C. *et al.* Quantity and quality of trabecular bone in the femur are enhanced by a strongly anabolic, noninvasive mechanical intervention. *J Bone Miner Res* **17**, 349-357, doi:10.1359/jbmr.2002.17.2.349 (2002).

73   Rubin, C., Xu, G. & Judex, S. The anabolic activity of bone tissue, suppressed by disuse, is normalized by brief exposure to extremely low-magnitude mechanical stimuli. *FASEB J* **15**, 2225-2229, doi:10.1096/fj.01-0166com (2001).

74   Pongkitwitoon, S., Uzer, G., Rubin, J. & Judex, S. Cytoskeletal Configuration Modulates Mechanically Induced Changes in Mesenchymal Stem Cell Osteogenesis, Morphology, and Stiffness. *Scientific reports* **6**, 34791, doi:10.1038/srep34791 (2016).

75   Uzer, G., Pongkitwitoon, S., Ete Chan, M. & Judex, S. Vibration induced osteogenic commitment of mesenchymal stem cells is enhanced by cytoskeletal remodeling but not fluid shear. *Journal of Biomechanics* **46**, 2296-2302, doi:10.1016/j.jbiomech.2013.06.008 (2013).

76   Uzer, G. *et al.* Sun-mediated mechanical LINC between nucleus and cytoskeleton regulates betacatenin nuclear access. *J Biomech* **74**, 32-40, doi:10.1016/j.jbiomech.2018.04.013 (2018).

77   Thompson, M., Woods, K., Newberg, J., Oxford, J. T. & Uzer, G. Low-intensity vibration restores nuclear YAP levels and acute YAP nuclear shuttling in mesenchymal stem cells subjected to simulated microgravity. *NPJ microgravity* **6**, 35, doi:10.1038/s41526-020-00125-5 (2020).

78   Newberg, J. K., Schimpf, J., Woods, K., Davis, P. H. & Uzer, G. Isolated Nuclei Stiffen in Response to Low Intensity Vibration. *bioRxiv*, 2020.2004.2009.034546, doi:10.1101/2020.04.09.034546 (2020).

79   Touchstone, H. *et al.* Recovery of stem cell proliferation by low intensity vibration under simulated microgravity requires intact LINC complex *npj. Microgravity* **5**, doi:doi.org/10.1038/s41526-019-0072-5 (2019).

80   Birmingham, E. *et al.* Mechanical stimulation of bone marrow in situ induces bone formation in trabecular explants. *Ann Biomed Eng* **43**, 1036-1050, doi:10.1007/s10439-014-1135-0 (2015).

81   Papageorgiou, M., Föger-Samwald, U., Wahl, K., Kerschan-Schindl, K. & Pietschmann, P. Age- and Strain-Related Differences in Bone Microstructure and Body Composition During Development in Inbred Male Mouse Strains. *Calcified tissue international* **106**, 431-443, doi:10.1007/s00223-019-00652-8 (2020).

82   Silva, D. *et al.* Biocompatibility, biodegradation and excretion of polylactic acid (PLA) in medical implants and theranostic systems. *Chemical Engineering Journal* **340**, doi:10.1016/j.cej.2018.01.010 (2018).

83   Xu, X., Jha, A., Harrington, D., Farach-Carson, M. & Jia, X. Hyaluronic Acid-Based Hydrogels: From a Natural Polysaccharide to Complex Networks. *Soft matter* **8**, 3280-3294, doi:10.1039/C2SM06463D (2012).

84   Blaber, J., Adair, B. & Antoniou, A. Ncorr: Open-Source 2D Digital Image Correlation Matlab Software. *Experimental Mechanics* **55**, 1105-1122, doi:10.1007/s11340-015-0009-1 (2015).

85   Lund, A. W., Stegemann, J. P. & Plopper, G. E. Mesenchymal Stem Cells Sense Three Dimensional Type I Collagen through Discoidin Domain Receptor 1. *Open Stem Cell J* **1**, 40-53, doi:10.2174/1876893800901010040 (2009).
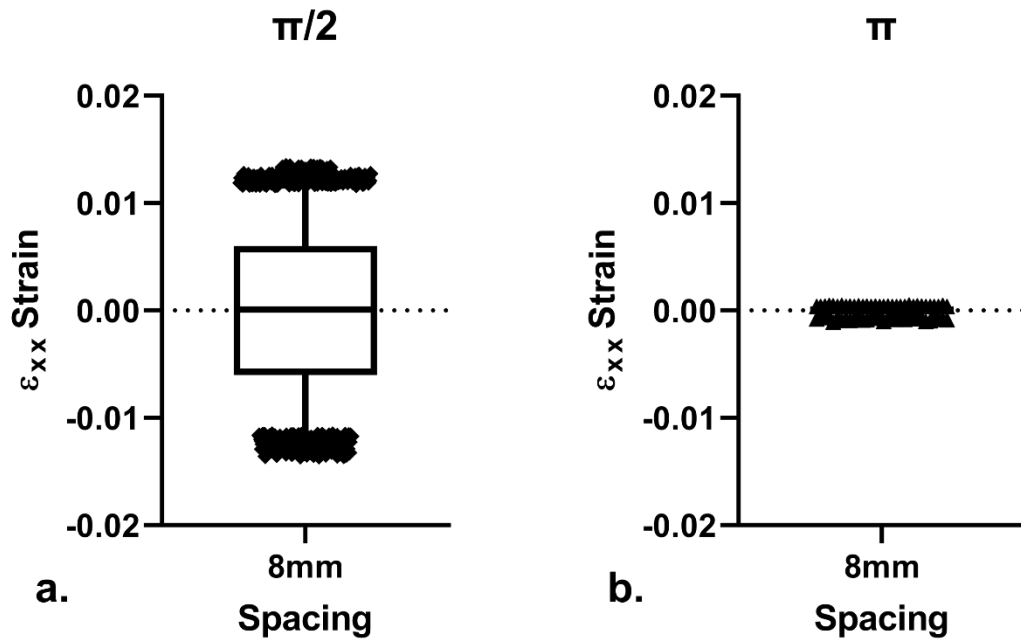
APPENDIX
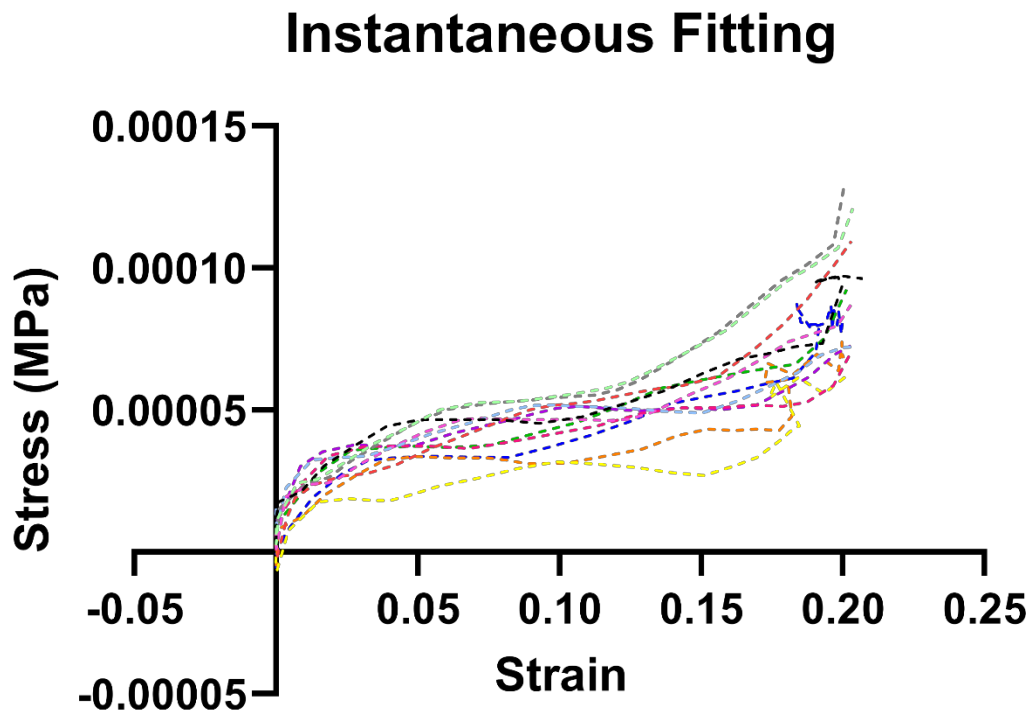
Supplementary Figure 1   Un-normalized instantaneous ramp fitting, showing that as the tests went on, the gel stiffened
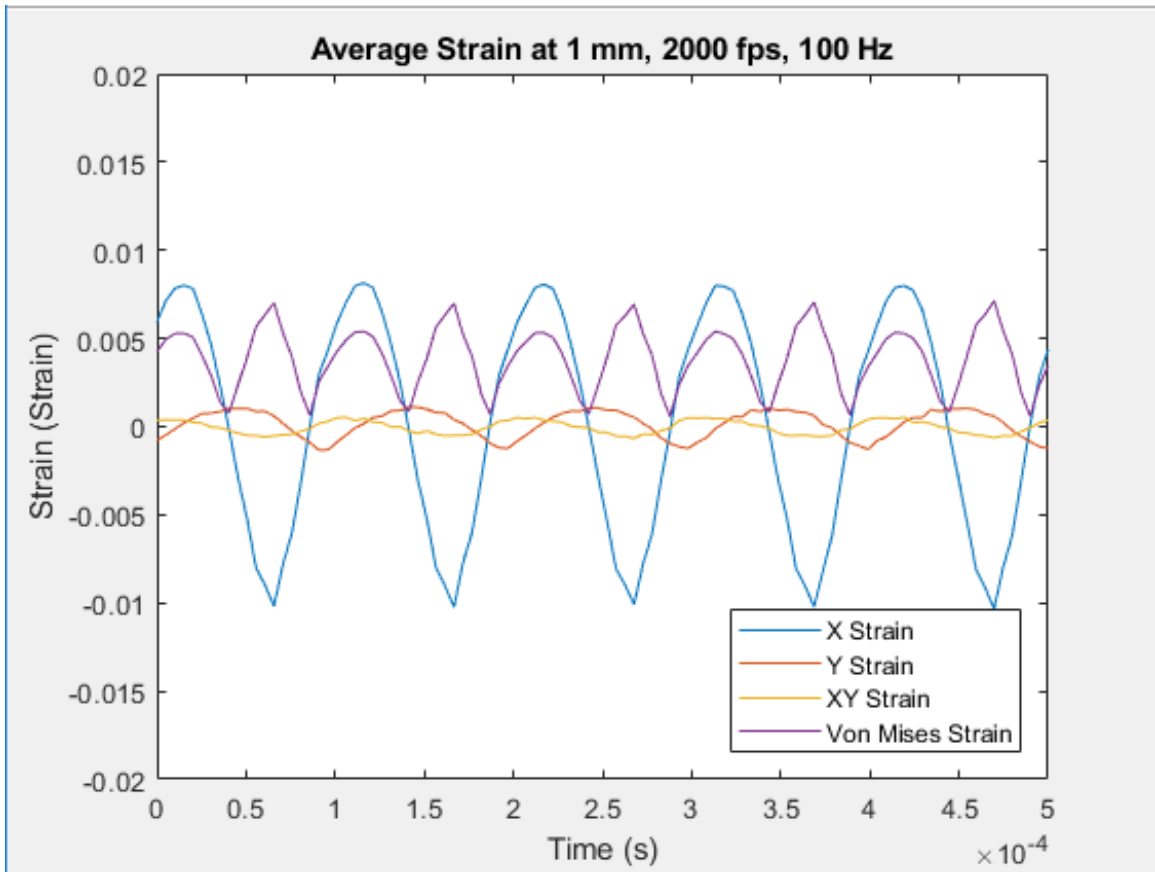
Supplementary Figure 2 **All tensor components of a vibrating well, with X strain being significantly larger than the Y and XY components**

Supplementary Figure 3 a) the strain distribution at π/2, which was used in the data processing b) data at π, which was the middle zero region
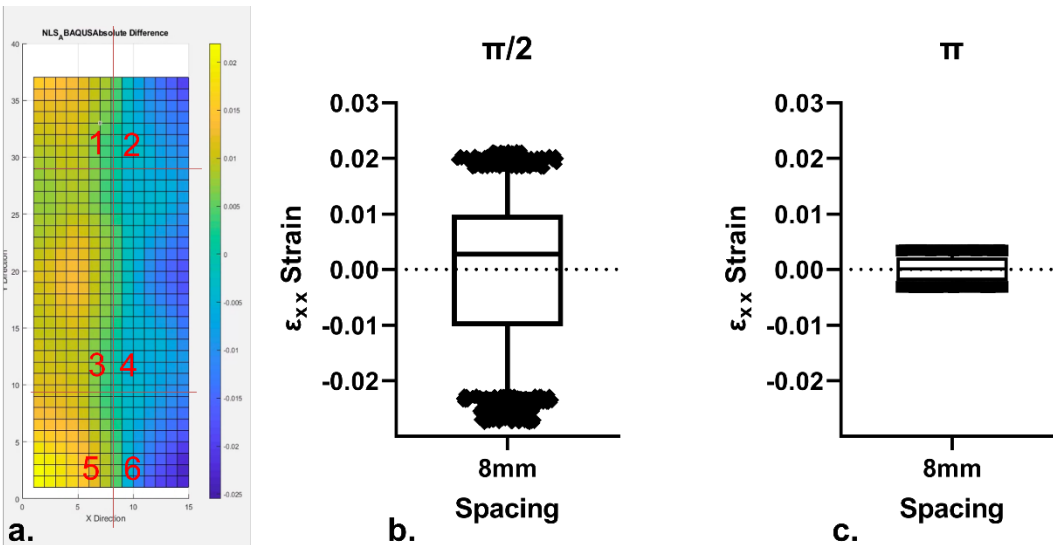
Supplementary Figure 4 a) strain difference between the experimental and FE model for hyaluronic acid b) the strain distribution at π/2 in the HA gel, which was used in the data processing b) data at π in the HA gel, which was the middle zero region, showing that less of the maximum points were at the extremes
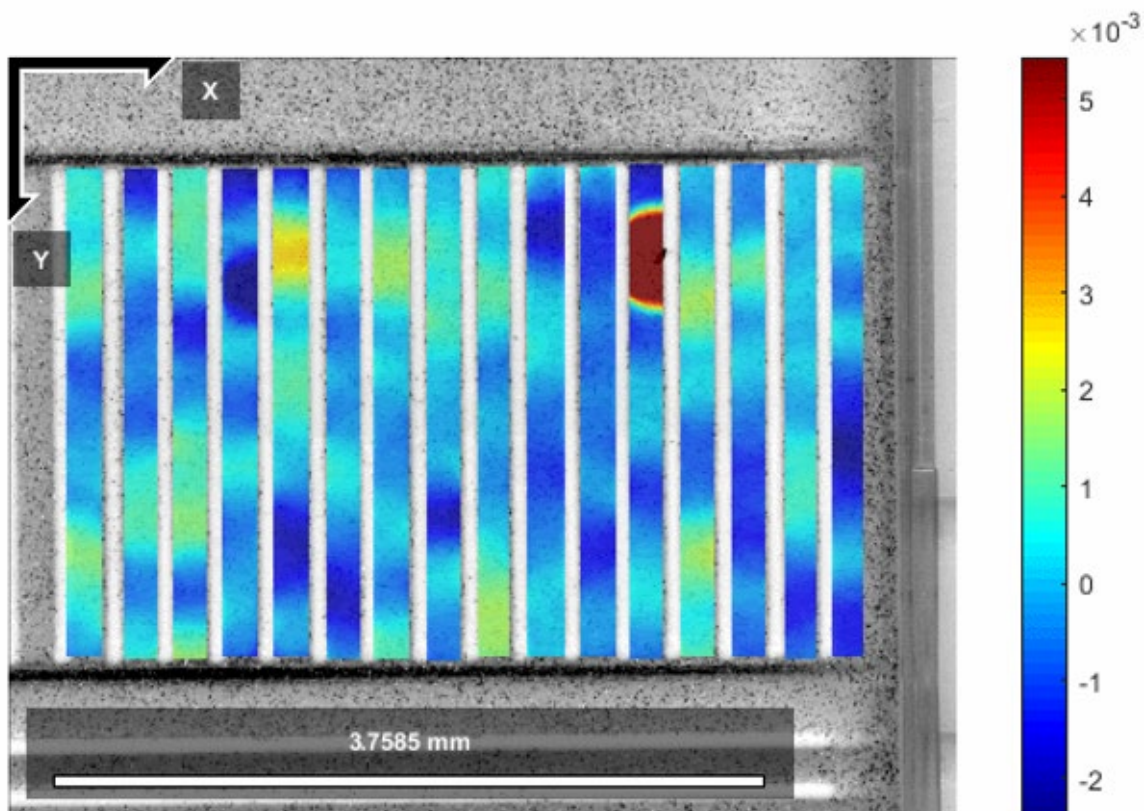
Supplementary Figure 5   early model of vibrating wells, in which there is interference transferred through the walls, into each of the wells.

Supplementary Tables

Supplementary Table 1   **HA Design of Experiments**

Friction	Damping	RMSE
10	0.3	0.28
10	0.003	0.29
0.01	0.3	0.28
0.01	0.003	0.38
0.01	3	0.25
0.001	3	0.35
0.75	0.03	0.28